Screens, streaks, and transition

David A. Pook†, Jonathan H. Watmuff and Adrian A. Orifici

School of Aerospace, Mechaical & Manufacturing Engineering, RMIT University, Bundoora, VIC 3083, Australia

(Received ?; revised ?; accepted ?. - To be entered by editorial office)

Defining a link between wind tunnel settling chamber screens, flow quality, and test-section boundary layer spanwise variation is necessary if accurate transition prediction is to be made. The aim of this work is to begin establishing this link. To achieve this, the computed, steady laminar wake of a zither (screen model) with imperfect wire spacing, is tracked through a contraction and into a model test-section. The contraction converts the zither wake into streamwise vorticity which then creates spanwise variation (streaks) in the test-section boundary layer. The magnitude of the spanwise variation is sensitive to the zither open-area ratio and imperfection, but the observed wavelength is relatively insensitive to the zither wire spacing. Increased spanwise variation is attributed to large wavelength variation of drag across the zither and not the coalescence of jets phenomena. The streaks in the boundary layer are compared to Klebanoff streaks and their influence on the boundary layer linear stability is predicted using the Parabolized Stability Equations and the e^N method. A standard deviation of zither wire position error of 38.1 μm (15% of wire diameter) for a zither of 50% open-area ratio is predicted to create streaks that could delay transition due to Tollmien-Schlichting growth by more than 10%.

Key words: Authors should not enter keywords on the manuscript, as these must be chosen by the author during the online submission process and will then be added during the typesetting process (see http://journals.cambridge.org/data/relatedlink/jfm-keywords.pdf for the full list)

1. Introduction

Thirty five years ago, Morkovin (1979) summarised observations of streamwise vorticity in boundary layers and the absence of a causative condition, although an empirical link to wind tunnel settling chamber screens had been established. Even today, experiments on nominally two-dimensional flows in wind tunnels cannot be assumed two-dimensional. Streamwise vorticity generates spanwise variation (streaks) that can significantly alter the boundary layer properties and stability characteristics. At elevated free-stream turbulence (FST) levels, the streaks are called Klebanoff streaks and transition to turbulence is often via a bypass mechanism. However, even at low FST levels significant spanwise variation and streaks can be observed in some experiments. The spanwise variation in the layer is not directly attributed to any particular measure or structure of the free-stream. Perhaps most importantly, transition results in different wind tunnels can quantitatively disagree and differ significantly to results obtained in the intended operating environment (e.g. flight), frustrating the engineer and creating uncertainty.

† Email address for correspondence: d.pook.engineer@gmail.com

1.1. *Observations of boundary layer spanwise variation*

Spanwise boundary layer variation can manifest in differing ways. The spanwise spacing of Görtler vortices is often varied and linked to the free-stream (Swearingen & Blackwelder 1987). Early studies by Klebanoff *et al.* (1961) noted significant spanwise variation in the boundary layer transition region. Recent theoretical advances have shown this to be a secondary instability of the Tollmien-Schlichting (TS) wave (Herbert 1988). However, the presence of weak streaks in the layer can affect the spanwise scale and growth rate of this secondary instability, and delay or promote transition (Liu *et al.* 2008*b*). A clear graphical demonstration of this can be seen in the LES simulations of Schlatter *et al.* (2011).

Elevated free-stream turbulence levels are associated with Klebanoff streaks, an unsteady, low-frequency disturbance that grows downstream (Klebanoff 1971; Kendall 1985; Westin *et al.* 1994; Kendall 1998; Watmuff 1998; Matsubara & Alfredsson 2001; Fransson *et al.* 2005*b*; Nolan & Walsh 2012). While free-stream disturbances are the cause of Klebanoff streaks, a direct connection between Klebanoff streaks, the free-stream, and a given wind tunnel's screens is still tenuous. Despite the low frequency and sometimes spanwise invariant location, research has focused on FST as the cause.

The presence of the Klebanoff streaks has been observed to significantly alter the location and mechanism of transition (Boiko *et al.* 1994; Watmuff 1998; Fransson *et al.* 2005*b*; Schlatter *et al.* 2008; Nolan & Walsh 2012). Strong Klebanoff streaks often result in transition by processes described as bypass transition (Morkovin 1969) although the term bypass is not synonymous with a single, well-defined transition process. Recent work has described how streaks in the Blasius layer may develop a secondary instability and undergo transition, a form of bypass transition (Andersson *et al.* 2001; Brandt & Henningson 2002; Asai *et al.* 2002; Schlatter *et al.* 2008; Hack & Zaki 2014). Recent experiments involving steady streaks and TS has shown reduced TS growth and transition delay (Fransson *et al.* 2005*a*; Shahinfar *et al.* 2012), although the experiment of Kendall (1991) and computations by Vaughan & Zaki (2011) shown streaks can also increase TS growth in some unknown circumstances.

Turbulent boundary layers are also affected by spanwise variation. Unexplained spanwise variation in both the tripped and non-tripped turbulent layers used to generate a mixing flow has been observed by Bell & Mehta (1990). Dengel & Fernholz (1989) found spanwise variation in the turbulent layer and showed direct linkage to the settling chamber screens by rotating them. Spanwise variation was considerably reduced by replacing the existing screen with one constructed from perforated metal. Recent examples include the unexplained spanwise variation in boundary layers growing over rough walls (Reynolds *et al.* 2006), and unexplained spanwise asymmetry when conducting experiments on riblet-type surface roughness (Nugroho *et al.* 2013). It was speculated that weak spanwise variation in the mean flow resulting from screens upstream of the wind-tunnel contraction might be the cause.

1.2. *Spanwise variation empirically linked to settling chamber screens*

Wind tunnel settling chamber screens and honeycomb are used to reduce FST levels and improve flow quality, yet many experimentalists identify them as directly influencing the test-section boundary layer. Bradshaw (1965) studied the tripped, turbulent boundary layer on the test-section floor that exhibited spanwise variation of skin-friction in excess of 10%. The spanwise variation was dependent on the individual screen, its orientation, and was repeatable when the open-area ratio was greater than 57%. Decreasing the open-area ratio below 57% produced a boundary layer with considerably increased spanwise variation. This was attributed to a spatial flow instability downstream of the screen called

the coalescence of jets. The coalescence of jets is a local change of flow pattern that occurs downstream of low open-area ratio zithers. Requiring screens to have an open-area ratio greater than 57% has become an accepted rule of thumb when selecting screens for wind tunnels.

Crow (1966) in response to the findings of Bradshaw (1965), analytically investigated the effect of small, steady spanwise variation of transverse velocity above a laminar boundary layer. Small velocity variations could create spanwise variation in the boundary layer. Extensive tests by de Bray (1967) experimentally confirmed the findings of Bradshaw (1965). High quality honeycomb was also observed to produce a more spanwise uniform boundary layer than the screens tested while locating the test-section plate on the wind tunnel centreline could reduce the spanwise variation by 50% compared to the wind tunnel wall boundary layer. De Bray (1967) concluded that immeasurable non-uniformities introduced by screens persist into the test-section and affect the spanwise variation of the layer. He postulated vortices of opposite rotation (apparently streamwise oriented) originate from adjacent openings in the screen and bundle together (coalesce) downstream. Similarly, Patel (1964) observed reduced spanwise variation when using honeycomb downstream of the settling chamber screens although this configuration is discouraged by some researchers as it can increase FST levels (Mehta & Bradshaw 1979). Increased spanwise variation was also observed with dust accumulation on the screens, underscoring the sensitivity of the test-section layer to screen quality.

The widespread consensus is that jets emanating from the screen openings, coalesce downstream of the screen due to some 'instability' formed at low open-area ratios. From this instability streamwise vortices form (de Bray 1967; Mehta & Bradshaw 1979) which persist through the contraction to the test-section layer. However, Mehta & Hoffmann (1987) found increased spanwise variation does not always correlate directly with an open-area ratio of 57%. Two screens, both with an open-area ratio of 58.8%, created spanwise skin friction variation of 10% and 18%. They concluded the 57% open-area ratio criteria is not sufficient to guarantee two-dimensionality of the test-section boundary layer. Mehta (1985) also tested screens of varying material and construction method. Plastic screens were found to produce less spanwise variation relative to woven metal screens.

Increased spanwise variation of the test-section boundary layer can also be associated with increased FST levels. Klebanoff (1971)† elevated the FST level in a wind tunnel with grids constructed of rope that were placed upstream of the contraction. A low frequency, spanwise thickening and thinning of the layer (spanwise variation) was observed that grew with increasing FST levels (Klebanoff streaks). However, the measurements of Watmuff (1998) suggest the link between FST and Klebanoff streaks is not simple. Watmuff found that replacing and tensioning the settling chamber screens reduced the FST level from 0.12% to 0.08%, but the Klebanoff streaks in the boundary layer (measured by u_{rms}) decreased by a factor of three. The unsteadiness in the layer was not spanwise uniform but clustered into 'clump' regions that did not shift with time. The unsteadiness in the layer was reduced by a further factor of two by simply reordering the screens based on quality as measured from laser scans, from least uniform (worst quality) to most uniform (best quality) downstream.

Westin *et al.* (1994) compiled published results of Klebanoff streak, streamwise growth and found considerable differences even when scaled with the FST level. However, the observed spacing of Klebanoff streaks generally shows a more reasonable agreement, approximately twice the boundary layer thickness ($\sim 2\delta_{99}$). Matsubara & Alfredsson (2001)

† Original source not obtained. The work is not formally published. All citations to this work are based on the summary by Kendall (1998)

observed the physical spacing of Klebanoff streaks to be independent of the mesh spacing used in the construction of a grid placed in the test-section to elevate the FST levels, however streak spacing has been found to be dependant on the free-stream environment (Fransson & Alfredsson 2003; Ovchinnikov *et al.* 2008).

Swearingen & Blackwelder (1986) found the 'natural' spacing of Görtler vortices to be very sensitive to the settling chamber screens. The apparent spacing was independent of the screen mesh spacing, test-section width, distance of the last screen from the contraction, and FST variation created by the removal of the honeycomb upstream of the screens. However, the observed spanwise pattern of Görtler vortices was stationary in time and strongly dependent on the downstream screen. Vertical cylinders oriented normal to the test-section leading edge and placed in the tunnel-contraction were used to alter the wake. Cylinder spacing larger than the natural Görtler spacing did not substantially alter the spanwise pattern, but the cylinder wakes were clearly visible in the boundary layer as narrow regions superimposed on the 'natural' pattern. Reducing cylinder spacing created a near periodic variation that approximated the cylinder spacing. The mechanism for the cylinder wake affecting the Görtler spacing was described as the creation of streamwise vorticity when the vortical wakes intersect the leading edge and are stretched by the boundary layer.

All of these observations clearly link settling chamber screens with spanwise variation in the test-section boundary layer and establish screen open-area ratio and quality as casual factors without any satisfactory explanation. Stationary Klebanoff streaks and Görtler vortices, and differing spanwise skin friction measurements depending on test-section plate location, questions any assumption of a homogeneous screen wake and FST across a wind tunnel cross-section.

1.3. *Flow downstream of screens*

The classical analysis of Taylor & Batchelor (1949) considered the linear, inviscid flow of streamlines through a gauze (screen) where a pressure drop takes place. A pressure drop of 2.76 was predicted to remove any mean streamwise flow non-uniformity. Decreasing screen open-area ratio will increase its pressure drop. Hancock (1998) extended the analysis to multiple screens and found no series of screens can perfectly attenuate free-stream non-uniformity, although any series of screens can give significant attenuation if the sum of the pressure drops is greater than 2.5. Bradshaw (1965) recommended screens should have a pressure drop less than 1.6 to avoid jet coalescence. This is significantly lower than analysis of Taylor & Batchelor (1949) indicates is required to achieve uniform flow. Schubauer *et al.* (1950) and Bradshaw (1965) have recommended a series of lower pressure drop screens be used to achieve a high pressure drop.

Morgan (1960) provides a short summary of early work on the coalescence of jets behind screens and zithers of low open-area ratio. Important points are that the instability occurs for open-area ratios less than approximately 50%, and that imperfections of the screen (quality) had been postulated as a possible cause. Earlier experimental work by Bohl (1940)† studied the flow downstream of a zither constructed of sharp wooden slats and provided the first analytical treatment of the coalescence of jets. Stable flow (no coalescence of jets) was observed for an open-area ratio of 63% and unstable flow (with coalescence of jets) for an open-area ratio of 50%. An analytical analysis was provided but Corrsin (1944) has criticised it for unclear physical assumptions in the derivation, although the results show qualitative agreement with experiment. Observations of the

† The original work is in German and the current authors can not directly review it. The review is based on the reading of Morgan (1960) and Corrsin (1944).

coalescence of jets have shown the flow pattern can be either stable in time or variable, and that multiple jets can coalesce at very low open-area ratios (Cheng & Moretti 1988; Le Gal *et al.* 1996).

Böttcher & Wedemeyer (1989) examined the steady wakes of screens and zithers as the sum of each individual wire's wake, governed by the linear diffusion equation. It should be noted that the coalescence of jets is equivalent to the merging of wakes (Corrsin 1944). The wake strength and wavelength of a zither was derived by considering each individual wire being randomly perturbed from its position in a zither with perfect wire spacing. Direct comparison between theory and the experiment was not possible as inputs to the wake strength formula had to be estimated. Their analysis offers the potential to relate screen quality to the downstream wake.

The wake turbulence of a screen is also affected by the open-area ratio and the coalescence of jets. Loehrke & Nagib (1972) and Tan-Atichat *et al.* (1982) found the decay of turbulent energy downstream of a low open-area ratio (30%) perforated plate was greatly reduced relative to plates with open-area ratios of 51% and 58%. They suggest the coalescence of jets may be responsible. Irregularities were also observed in the mean flow far downstream. Previously, Schubauer *et al.* (1950) had noted that low open-area ratio screens (high pressure drops) could produce abnormally large streamwise velocity fluctuations and less uniform mean flow, but the cause was not identified. Recent computations by Ertunç *et al.* (2010) show turbulence downstream of a symmetric (perfect) screen is not homogeneous. If the screen has small non-uniformity in its construction (variation in wire position) then the mean flow is also non-homogeneous.

No satisfactory explanation exists for the coalescence of jets, nor does the traditional inviscid analysis of screens predict its appearance or effects. To the authors knowledge, there has been no direct observation of the coalescence of jets for a screen (as opposed to a zither) and all reports of increased spanwise variation attributed to this phenomena have not directly observed its occurrence. How the change in flow pattern at a screen, located far away and upstream of a contraction which produces near uniform streamwise velocity mean-flow, increases spanwise variation of the test-section layer not fully explained.

1.4. *Creating the link to settling chamber screens*

Explaining the creation of spanwise variation and streaks in the boundary layer requires understanding how disturbances grow in the layer, the receptivity of disturbances, the evolution of the disturbance in the free-stream from their source, and the creation of the disturbances at a source (screen). Recent work has often focused on streak growth via non-modal theories (Andersson *et al.* 1999; Luchini 2000; Schmid 2007) or transient/algebraic growth (Ellingsen & Palm 1975; Reddy *et al.* 2008; Hultgren & Gustavsson 1981; Butler & Farrell 1992) Asymptotic analyses have linked Klebanoff streaks to FST (Leib *et al.* 1999; Wundrow & Goldstein 2001; Ricco 2009; Ricco *et al.* 2011) and highlighted the importance of the free-stream anisotropy. Goldstein *et al.* (1992) and Goldstein & Leib (1993) describe the receptivity of normal and streamwise vorticity that creates streaks while the computations of Schrader *et al.* (2010) and Pook & Watmuff (2014) demonstrate the preference for the receptivity of streamwise vorticity. Pook & Watmuff (2014) have also demonstrated how normal vorticity entering a wind tunnel contraction can be tilted and stretched into significant streamwise vorticity at the exit, away from the wind tunnel centreline. This is consistent with the observations by de Bray (1967) of increased skin friction variation away from the wind tunnel centreline, suggesting the tilting and stretching of normal vorticity in the contraction is a significant mechanism in the generation of spanwise variation of the test section boundary layer and Klebanoff streaks. Any analysis that attempts to link spanwise variation to the settling chamber screens must

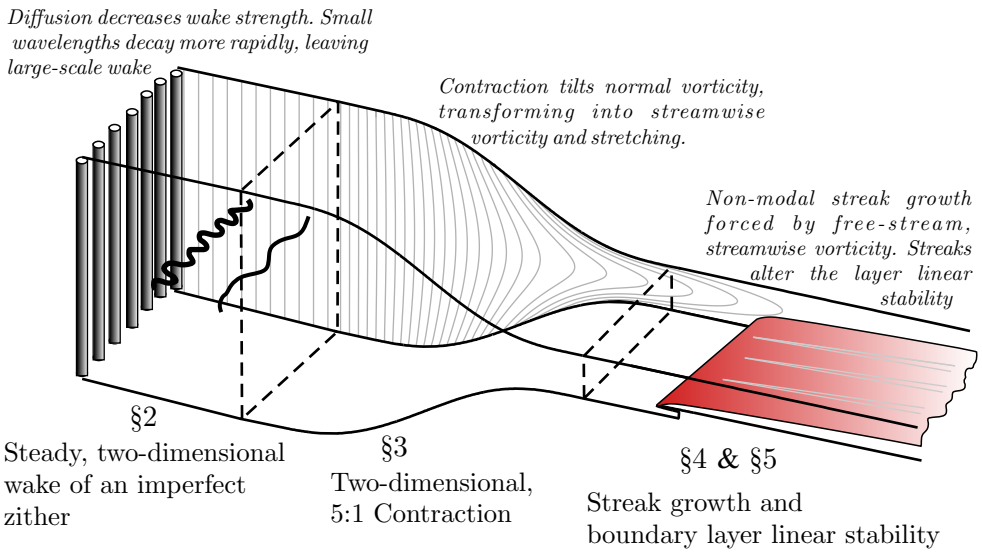

FIGURE 1. Overview of geometry and section breakdown.

consider the contraction. Recreating streaks that link directly to a physical wind tunnel source may also be important for determining their affect on the boundary layer stability and transition.

1.5. *Overview*

The work to be presented will track a steady vortical disturbance, generated at a zither of wires located upstream of a contraction, all the way to the test-section boundary layer. The streaks generated will be documented and the predicted effect on transition assessed. The work is divided into the following sections:

(i) §2 examines the steady laminar wakes of an imperfect zither, extending the analysis of Böttcher & Wedemeyer (1989). It will be shown that substantial variation of drag across a zither can lead to a reduced wake decay rate but this decay rate is not so easily realised.

(ii) §3 will pass the wakes through a 5:1, two-dimensional contraction. This will create streamwise vorticity at the exit via tilting and stretching of normal vorticity.

(iii) §4 will pass the wakes exiting the contraction over a flat-plate boundary layer. The streamwise vorticity present will create steady streaks with the characteristics of Klebanoff streaks.

(iv) §5 will examine the linear stability of the test-section streak base-flows.

The geometry for the contraction and test-section leading edge shape and position is the same as used in Pook (2013) and Pook & Watmuff (2014). An overview is provided in figure 1.

Modelling a zither is computationally cheaper than a screen, yet it captures many experimental observations and provides an initial step towards Morkovin's call to link screens with the test-section layer. The simplification to steady, laminar flow is justified by the stationary Klebanoff streaks and Görtler vortices observed by Watmuff (1998) and Swearingen & Blackwelder (1986) at low FST levels. The current work is strictly applicable to zithers with steady laminar wakes. However, qualitative similarities with observations made from screens will be noted and the concepts explored will be implied to be valid for screens without direct proof.

2. The steady laminar wake of a zither

The (simplified) governing equation of a far wake is the linear diffusion equation (Batchelor 2000; Böttcher & Wedemeyer 1989),

$$Uu_x = \nu u_{zz}, \tag{2.1}$$

where $u = u(x, z)$ is the streamwise velocity of the wake, U the uniform free-stream flow, and ν is the fluid kinematic viscosity. Considering a spanwise (z) periodic domain of width L and a zither with N wires, it can be shown the solution to (2.1) is,

$$u(x, z) = \sum_{k=-\infty}^{\infty} a_k \exp\left(\frac{2\pi i k z}{L}\right) \exp\left(-4\pi^2 K^2 \overline{x}\right), \tag{2.2}$$

where a_k are the unknown Fourier coefficients, k is the integer wavenumber, Re_M is the Reynolds number based on the perfect zither wire spacing (M), K is k/N, and $\overline{x}$ is a non-dimensional streamwise distance defined by,

$$\overline{x} = \frac{x}{M}\frac{1}{Re_M}. \tag{2.3}$$

The wake energy is found as,

$$\overline{u^2} = \frac{1}{L}\int_0^L (U-u)^2\, dz = \sum_{k=-\infty}^{\infty} |a_k|^2 \exp\left(-8\pi^2 K^2 \overline{x}\right), \tag{2.4}$$

where the $k = 0$ mean flow mode is not included in the summation. The downstream decay of a given mode k is described by the exponential term in (2.2),

$$\text{decay} = \exp\left(-4\pi^2 K^2 \overline{x}\right). \tag{2.5}$$

As k increases (wavelength decreases), the decay rate with streamwise distance x is increased non-linearly.

2.1. *Summation of wakes*

The wake of a zither will be considered as the summation of each individual wire's wake. Unlike Böttcher & Wedemeyer (1989), each wire will be assumed to have an individual wake. Each wake is given by an unknown function, $W_n(z - z_n)$, where z_n is the spanwise location of the n^{th} wire. The wake of the zither at $\overline{x} = 0$ (initial condition) is found as,

$$u(0, z) = \sum_{n=1}^{N} W_n(z - z_n), \tag{2.6}$$

The Fourier coefficients of (2.2) are determined by substituting (2.6) into (2.2), giving,

$$a_k = \frac{1}{L}\int_0^L \sum_{n=1}^{N} W_n(z - z_n) \exp\left(\tfrac{-2\pi i k z}{L}\right) dz. \tag{2.7}$$

Far downstream the wavelengths are large in comparison to the wire spacing as observed by Böttcher & Wedemeyer (1989). They argue the wake function of a wire can be considered as a point source,

$$\int W_n(z - z_n) = q_n \delta(z - z_n), \tag{2.8}$$

where $\delta(z - z_n)$ is the Dirac function and q_n is the source strength of the n^{th} wire. The Fourier coefficients are then,

$$a_k = \frac{1}{L}\sum_{n=1}^{N} q_n \exp\left(\frac{-2\pi i k z_n}{L}\right). \tag{2.9}$$

Every wire in the zither is perturbed from its perfect position (Mn), giving the position of the n^{th} wire as,

$$z_n = M(n + \delta_n), \tag{2.10}$$

where δ_n is a non-dimensional random variable, $\delta \ll M$. The source strength of each wire (q_n) is expressed in-terms of the mean source strength $(\overline{q})$ by,

$$q_n = \overline{q}(1 + a_n), \tag{2.11}$$

where a_n is a non-dimensional random variable with zero mean by definition. Substituting (2.10) and (2.11) into (2.9) gives the Fourier coefficients as,

$$a_k = \frac{\overline{q}}{L}\sum_{n=1}^{N}(1 + a_n)\exp\left(\frac{-2\pi i k M(n + \delta_n)}{L}\right). \tag{2.12}$$

Following Böttcher & Wedemeyer (1989), modes of large k will negligible in the far wake. This allows the exponent of (2.12) to be expanded with the first terms of the exponential power series $(e^x \approx 1 + x)$ and modes that are an integer multiple of N to be neglected leaving,

$$a_k = \frac{\overline{q}}{NM}\sum_{n=1}^{N}(2\pi i K\delta_n + a_n - 2\pi i K a_n\delta_n)\exp(-2\pi i K n). \tag{2.13}$$

2.2. *Predicted wake from a zither with imperfect wire spacing and source strength*

The Fourier coefficients of a zither with both variation in wire position and source strength can be factored as,

$$a_k = -2\pi K A(k) + B(k), \tag{2.14}$$

where $A(k)$ contains the summations of $i\delta_n$ and $ia_n\delta_n$, and $B(k)$ contains the a_n summation. The mean wake energy is then,

$$\overline{u^2} = \frac{\overline{q}^2}{N^2M^2}\sum_{k=-\infty}^{\infty}\left(4\pi^2K^2AA^\dagger + BB^\dagger + 4\pi K\left(AB^\dagger + A^\dagger B\right)\right)\exp\left(-8\pi^2K^2\overline{x}\right), \tag{2.15}$$

where † represents complex conjugation. Assuming all wavelengths are excited relatively equally allows the summations to be replaced with their mean values,

$$\overline{AA^\dagger} = N\sigma_\delta^2 + N\mu_\delta^2 + N\sigma_{\delta a}^2 + N\mu_{\delta^2 a}, \quad \overline{BB^\dagger} = N\sigma_a^2, \quad \overline{AB^\dagger + A^\dagger B} = 0, \tag{2.16}$$

where,

$$\sigma_\delta^2 = \frac{1}{N}\sum_{n=1}^{N}\delta_n^2, \quad \sigma_a^2 = \frac{1}{N}\sum_{n=1}^{N}a_n^2, \quad \mu_\delta = \frac{1}{N}\sum_{n=1}^{N}\delta_n,$$
$$\sigma_{\delta a}^2 = \frac{1}{N}\sum_{n=1}^{N}\left(\delta_n a_n\right)^2, \quad \mu_{\delta^2 a} = \frac{1}{N}\sum_{n=1}^{N}\delta_n^2 a_n. \quad (2.17)$$

Following Böttcher & Wedemeyer (1989), the means are substituted into (2.15) and considering an infinite zither ($N \to \infty$, $k/N \to K$) allows the summation to be replaced with the integral,

$$\overline{u^2} = \frac{\overline{q}^2}{M^2}\int_{-\infty}^{\infty}\left(4\pi^2K^2\left(\sigma_\delta^2 + \mu_\delta^2 + \sigma_{\delta a}^2 + \mu_{\delta^2 a}\right) + \sigma_a^2\right)\exp\left(-8\pi^2K^2\overline{x}\right)dK. \quad (2.18)$$

Assuming $a_n \ll 1$ and $\delta_n \ll 1$, then terms involving their higher products can be neglected. The wavenumber with peak energy can be found from the integrand as,

$$K = \frac{1}{2\sqrt{2}\pi\overline{x}}\sqrt{\overline{x} - 2\frac{\sigma_a^2}{\sigma_\delta^2}\overline{x}^2}, \quad (2.19)$$

giving the dominant wake wavelength as,

$$\frac{\lambda}{M} = \frac{2\sqrt{2}\pi\overline{x}}{\sqrt{\overline{x} - 2\frac{\sigma_a^2}{\sigma_\delta^2}\overline{x}^2}}. \quad (2.20)$$

Near the zither (small $\overline{x}$) or when σ_a is small, the wavelength will be independent of the zither geometry giving,

$$\frac{\lambda}{M} = \sqrt{8\pi^2\overline{x}}, \quad (2.21)$$

as originally derived by Böttcher & Wedemeyer (1989). With increasing $\overline{x}$ and $\sigma_a \neq 0$, the $\overline{x}^2$ term will dominate and the predicted wavelength will asymptote to infinity at,

$$\overline{x} = \frac{1}{\sqrt{2}}\frac{\sigma_\delta}{\sigma_a}. \quad (2.22)$$

Physically, this is the change from the well-defined peak wavelength to the $k = 0$ mode. However, the wake component $k = 0$ mode has zero energy. The $k = 1$ mode will have the greatest energy.

The mean energy of the wake is found as the solution of (2.18). The average wake strength non-dimensionalised by U is then,

$$\Delta u = \sqrt{\frac{0.2233^2\overline{q}^2\left(\sigma_\delta^2 + \mu_\delta^2 + \sigma_{\delta a}^2 + \mu_{\delta^2 a}\right)}{M^2U^2\overline{x}^{1.5}} + \frac{0.4466^2\overline{q}^2\sigma_a^2}{M^2U^2\overline{x}^{0.5}}}, \quad (2.23)$$

where Δu is defined as,

$$\Delta u = \frac{\sqrt{\overline{u^2}}}{U}. \quad (2.24)$$

Expecting $a_n \ll 1$ and $\delta_n \ll 1$, the wake strength due to a zither with imperfection in wire position and source strength, the combined wake strength equation, is derived as,

$$\Delta u = \frac{0.2233\overline{q}\sigma_\delta}{MU\overline{x}^{0.75}}\sqrt{1+4\frac{\sigma_a^2}{\sigma_\delta^2}\overline{x}}. \tag{2.25}$$

2.3. *Predicted zither wake from only imperfect wire positions*

Assuming each wire of the zither is identical and neglecting the change in wire source strength due to an error in position (all $a_n = 0$) then the Fourier coefficients of (2.13) are given by,

$$a_k = \frac{\overline{q}}{NM}\sum_{n=1}^{N} -2\pi iKk\delta_n \exp\left(-2\pi iKn\right). \tag{2.26}$$

The dominant wavelength of the zither wake is found as (2.21) and assuming $\mu_\delta^2 = 0$, the average wake strength of a zither with only imperfect wire position is,

$$\Delta u = 0.2233\frac{\overline{q}\sigma_\delta}{MU\overline{x}^{0.75}}, \tag{2.27}$$

as originally derived by Böttcher & Wedemeyer (1989).

2.4. *Predicted zither wake from only imperfect wire source strengths*

Assuming only imperfection of wire source strength gives the Fourier coefficients,

$$a_k = \frac{\overline{q}}{NM}\sum_{n=1}^{N} a_n \exp\left(-2\pi iKn\right). \tag{2.28}$$

The dominant wavenumber is found as $k = 0$, but as the wake has no zero mode, the $k = 1$ will dominate downstream. The average wake strength for a zither with imperfect wire source strength is found as,

$$\Delta u = 0.4466\frac{\overline{q}\sigma_a}{MU\overline{x}^{0.25}}. \tag{2.29}$$

2.5. *Differing zither wake decay rates*

The three wake strength formulas (2.25), (2.27) and (2.29) are compared in figure 2 for zithers with: imperfect wire spacing and source strength ($\sigma_\delta = \sigma_a = 0.05$); only imperfect wire position ($\sigma_\delta = 0.05$, $\sigma_a = 0$); and only imperfect source strength ($\sigma_\delta = 0$, $\sigma_a = 0.05$). The wake decay of a zither with only imperfect wire position differs significantly to a zither with only imperfect source strength, predominately due to the respective $\overline{x}^{-0.75}$ and $\overline{x}^{-0.25}$ dependencies. For the same standard deviation of imperfection, the wake of zither with only variation of wire source strength will be weaker close to the zither but stronger far downstream. The wake decay rates are explained by the Fourier coefficient distributions shown in figure 2. The distribution for a zither with only variation in wire position is approximated by,

$$a_{kP} = \frac{2\pi k\sigma_\delta\overline{q}}{M\sqrt{N}}. \tag{2.30}$$

The distribution for variation only in source strength is approximated as,

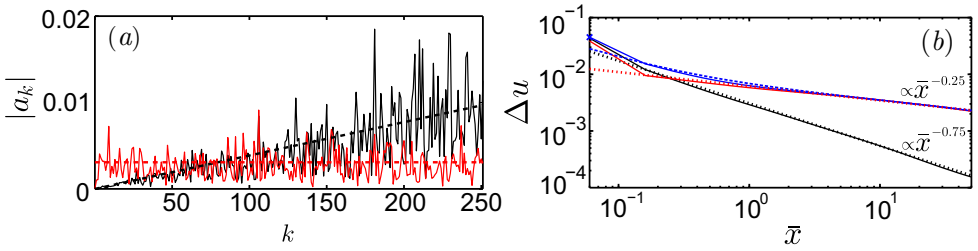

FIGURE 2. (a) Example Fourier coefficients at zither due to: —— Random normal distribution of wire drag; ----- Mean distribution of drag, (2.31); —— Random normal distribution of wire position; ----- Mean distribution of position, (2.30). (b) Example wake strengths: —— Random normal distribution of wire drag calculated with (2.28) and (2.4); ----- Variation of drag, (2.29); —— Random normal distribution of wire position calculated with (2.26) and (2.4); ····· Variation of position, (2.27); —— Random normal distribution of wire drag and position calculated with (2.13) and (2.4); ----- Variation of drag and position, the combine wake strength equation, (2.25). (colour online)

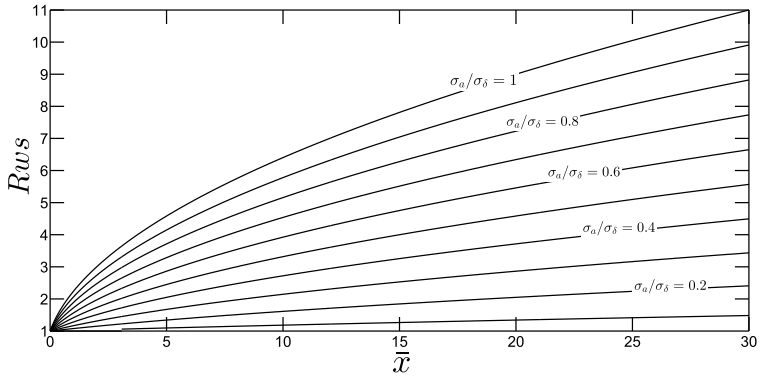

FIGURE 3. Relative wake strength (Rws) versus $\overline{x}$ for varying σ_a/σ_δ.

$$a_{kD} = \frac{\sigma_a \overline{q}}{M\sqrt{N}}. \tag{2.31}$$

Variation in wire source strength can create significantly larger small wavenumbers (large wavelengths), that decay slower and create a stronger far wake. The variation in wire position, and its importance relative to the variation in source strength when determining the wake strength (Rws), can be found by dividing (2.25) by (2.27) giving,

$$Rws = \sqrt{1 + 4\left(\frac{\sigma_a}{\sigma_\delta}\right)^2 \overline{x}}. \tag{2.32}$$

Equation (2.32) is plotted in figure 3 for varying σ_a/σ_δ. As an illustration, if the standard deviation of source strength is a 10% of the standard deviation of wire position, then the far wake at $\overline{x} = 15$ will be 26% stronger than for a zither with no variation in source strength (drag). This leads to a hypothesis that significant spanwise variation in the test-section boundary layer may be linked to screens that have significant spatial variation of source strength. This spatial variation may be induced by poor quality screens that have larger variations in wire position which, particularly for lower open-area ratios, may lead to nearby wires influencing each others source strength (drag) and create a stronger far wake.

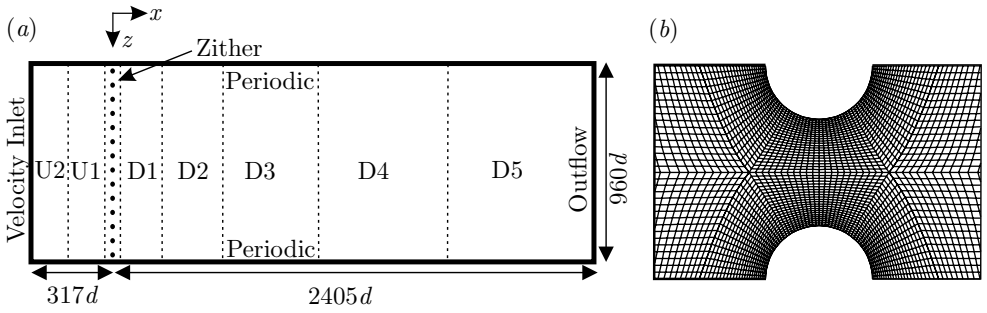

FIGURE 4. (*a*) Overview of the zither mesh domain. Marked regions start at streamwise positions: U2 at -317d, U1 at -76d, Zither at -7d to 7d, D1 at 7d, D2 at 67d, D3 at 205d, D4 at 405d, D5 at 805d. (*b*) Close-up of the CFD mesh between two wires. Every second line shown.

2.6. *Zither CFD domain and methods*

Navier-Stokes simulations (CFD) will be used to test the hypothesis that the variation in wire source strength (drag) across the zither, induced by variation in wire positions, will create a stronger far downstream wake. Ten zithers with differing combinations of open-area ratio and variation of random wire position error will be examined.

The steady, pressure-based solver (2nd-order upwind differencing for pressure, 3rd-order MUSCL differencing for momentum) of the ANSYS Fluent CFD package is used. Solution convergence is judged by the constancy of the far wake with increasing iteration and convergence of global residual monitors. An overview of the zither domain and mesh is shown in figure 4. The velocity-inlet boundary condition is 317d (80.47 mm) upstream of the zither while the outflow boundary condition is located at 2405d (610.8 mm). Periodic boundary conditions are used in the spanwise direction. The number of wires in the zither varies between 320 and 576, depending on the open-area ratio, and is listed in table 1. The spanwise domain is sized to provide enough wavelengths for the wake strength formulas derived to be representative.

To reduce the total mesh control volumes (CV) , eight regions with varying resolution are used as the wake spanwise scale increases. Each region is composed of structured quadrilateral CV aligned with the uniform flow direction. Hanging nodes are used to halve the number CV in the spanwise direction at each region boundary. Figure 4 shows the mesh between wires. There are 216 CV on the surface of a wire. Total mesh size varies between 23.4 and 44.2 million CV, depending on the open-area ratio. A simulation refining the mesh by a factor of two in each direction, within 10d of the zither, changes the calculated wire forces less than 0.5%.

2.7. *Zither geometry*

Table 1 lists the geometry parameters for all the zithers that are composed of circular wires arranged in a line perpendicular to the free-stream. All wires have a diameter (d) of 254 μm. The spanwise extent (L) of all zithers is 243.84 mm (960d). Four open-area ratios (β) are used, β =40%, 50%, 60%, 66.67%. The open-area ratio, diameter and the mesh spacing of the perfect zither (uniformly spaced wires) are related by

$$\beta = 1 - \frac{d}{M}. \tag{2.33}$$

Each wire (n) is randomly perturbed from its position in the perfect zither by some distance, introducing an error (ϵ) in position given by,

β	M	σ_δ	$\sigma_\delta M$	Re_M	N	$\overline{q}$	$\overline{C_d}$	σ_a	$\frac{\sigma_a}{\sigma_\delta}$	$\Delta u/U$ % at	
%	μm		μm		wires	$\times 10^{-3}$		$\times 10^{-3}$		$\overline{x}=10$	$x=2300d$
40.00	423.3	0.025	10.6	49	576	2.427	11.2	7.24	0.29	0.52	0.27
50.00	508.0	0.025	12.7	59	480	1.480	6.85	3.23	0.13	0.21	0.14
50.00	508.0	0.050	25.4	59	480	1.482	6.87	7.11	0.14	0.47	0.31
50.00	508.0	0.075	38.1	59	480	1.486	6.89	13.5	0.18	0.88	0.61
60.00	635.0	0.025	15.9	74	384	0.991	4.59	3.33	0.13	0.14	0.12
60.00	635.0	0.050	31.8	74	384	0.993	4.60	6.55	0.13	0.26	0.21
60.00	635.0	0.075	47.7	74	384	0.996	4.61	10.1	0.13	0.39	0.32
60.00	635.0	0.100	19.0	74	384	0.999	4.63	16.7	0.17	0.53	0.44
66.67	762.0	0.025	38.1	89	320	0.789	3.66	3.25	0.13	0.11	0.12
66.67	762.0	0.050	57.1	99	320	0.841	3.90	6.62	0.13	0.17	0.22

TABLE 1. Zither geometry, source strength data, and wake strength at $\overline{x}=10$ and $x=2300d$.

$$\epsilon_n = \delta_n M. \tag{2.34}$$

A normal distribution is used for the random variation of δ_n, with (near) zero mean and a given standard deviation (σ_δ) listed in table 1 (see Pook 2013 for quantile-quantile plots). The β=60% zithers share the same distribution of δ_n, i.e. the differing standard deviation is achieved by multiplying by a constant. The same applies for the $\beta = 66.67\%$ zithers. The $\beta = 50\%$ zithers all have differing distributions. A constant σ_δ implies a decreasing physical error in wire position with decreasing open-area ratio. The largest standard deviation in physical units for the zithers studied is 57.1 μm, or 22% of the wire diameter. The smallest is 10 μm, or 4% of the wire diameter. The uniform free-stream is $U = 1.7$ ms^{-1} giving a Reynolds number based on wire diameter (Re_d) of 29.6 for all zithers except the $\beta = 66.67\%$ with $\sigma_\delta = 0.05$ zither that uses $U = 1.9$ ms^{-1}.

2.8. *Wake strength*

The wake strength of the CFD zither simulations is compared with the predicted wake strength due only to variation in wire position (2.27), and the combined wake strength equation (2.25), in figure 5. Beyond $\overline{x} \gtrsim 0.1$, the CFD wakes decay as $\overline{x}^{-0.75}$ although the CFD wakes are 20% to 60% stronger than (2.27) predicts. Downstream of $\overline{x} \approx 2$, the decay of some wakes reduces slightly but not nearly as dramatically as (2.25) predicts. The lack of change is particularly evident for the $\beta = 40\%$ zither that has the largest value of σ_a/σ_δ but deviates little from $\overline{x}^{-0.75}$.

Table 1 shows that the mean wire source strength is (near) invariant to the standard deviation of wire position variation (σ_δ). The wire source strength is obtained from the CFD wire force data and the mean calculated by,

$$\overline{q} = \frac{1}{\rho U N} \sum_{n=1}^{N} D_n, \tag{2.35}$$

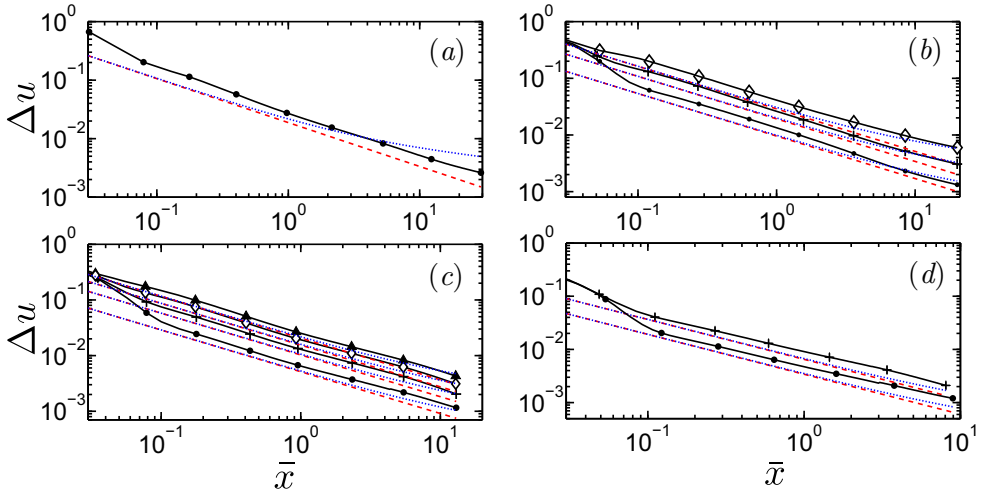

FIGURE 5. Zither wake strength from CFD simulations compared to prediction: (*a*) $\beta = 40\%$; (*b*) $\beta = 50\%$; (*c*) $\beta = 60\%$; (*d*) $\beta = 66.67\%$. Lines: ----- Prediction due to only position variation, 2.27; ····· Prediction of combined wake strength 2.25; —•— CFD wake for $\sigma_\delta = 0.025$; —+— CFD wake for $\sigma_\delta = 0.05$; —◇— CFD wake for $\sigma_\delta = 0.075$; —▲— CFD wake for $\sigma_\delta = 0.1$. (colour online)

where ρ is the fluid density and D_n is the drag force of the n^{th} wire. The drag coefficient (C_d) is defined as $D = 0.5\rho U^2 dC_d$. Table 1 shows σ_a/σ_δ is also near constant 0.13 for the $\beta = 60\%$ and $\beta = 66.67\%$ zithers when $\sigma_\delta \leqslant 0.05$. The wake strength at a given streamwise distance for the $\beta = 60\%$ and 66.67% zithers scales near linearly with σ_δ. However, the $\beta = 50\%$ zithers show linear scaling only for $\sigma_\delta = 0.025$ and 0.05. The $\sigma_\delta = 0.075$ zither wake strength is significantly greater than a linear scaling, indicating the wake strength due to only variation in wire position (2.27) does not predict the correct wake decay for zithers with large σ_δ that induces variations of drag across the zither. With decreasing open-area ratio, the ratio σ_a/σ_δ is seen to increase but only substantially for the $\beta = 40\%$ zither. However, its wake decay maintaining $\overline{x}^{-0.75}$indicates a flawed assumption in the derivation of the combined wake strength equation (2.25).

2.9. *Validity of the liner diffusion equation*

To validate the linear diffusion equation, the $\beta = 40\%$ zither CFD results are sampled downstream as an initial condition for (2.1). The predicted wake using the downstream initial condition is shown in figure 6. A downstream initial condition under predicts wake strength until a boundary condition at $\overline{x} = 2.5$ is used. At this position, the wake strength is approximately $\Delta u = 1\%$. Initial conditions sampled from velocity data close to the zither fail as pressure has not been recovered. Figure 7 shows the wavenumber (k) spectrum of the wake computed with a Fast Fourier Transform (FFT) of the streamwise velocity and pressure with varying $\overline{x}$ for the $\beta = 40\%$ zither. At $\overline{x} = 0.13$, the large wavelength components of pressure are substantial, i.e. there are large spanwise wavelength pressure variations. With increasing streamwise distance the pressure is recovered into the large wavelength components of the streamwise velocity and a downstream sampled boundary condition is accurate.

The wake strength using the Fourier coefficients calculated at the zither from wire position and drag data (i.e. initial condition at the zither) is seen to undershoot the CFD wake in the region $\overline{x} = 0.1$ to $\overline{x} = 6$ before showing reasonable agreement with the CFD in the remainder of the solution domain. This indicates the linear diffusion equation with known wire source strength can predict the far wake. The initial condition using

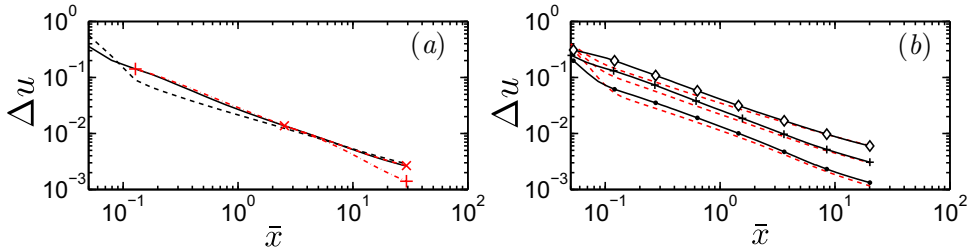

FIGURE 6. (*a*) The effect of a downstream initial condition for the $\beta = 40\%$, $\sigma_\delta = 0.025$ zither. —— CFD; ----- Calculated with (2.1) and (2.13); +·-·+ Calculated with (2.1) from initial condition at $\overline{x} = 0.13$; ×·-·× Calculated with (2.1) from initial condition at $\overline{x} = 2.5$. (*b*) $\beta = 50\%$ zithers CFD wake strength compared to calculation with (2.1) and (2.13). Lines and markers as for figure (2). (colour online)

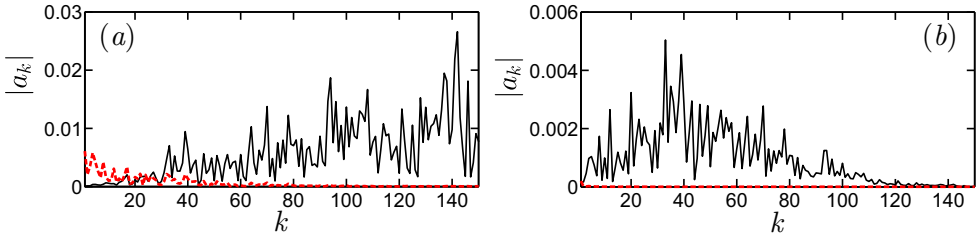

FIGURE 7. FFT of streamwise velocity and pressure for the $\beta = 40\%$, $\sigma_\delta = 0.025$ zither: (*a*) $\overline{x} = 0.13$; (*b*) $\overline{x} = 2.5$. Lines: —— Streamwise velocity; ----- Pressure (colour online).

wire position and drag data is accurate downstream as the drag component captures the pressure variation.

2.10. *Distribution of source strength (drag)*

The success of the linear diffusion equation (2.1) indicates a flawed assumption in the derivation of the combined wake strength equation. Figure 8 shows the Fourier spectra due to only variation in wire drag, calculated with (2.28), for the zithers. The magnitude of the $\beta = 60\%$ and 66.76% zither Fourier coefficients increase from $k = 0$, peak at approximately $k = 100$, before diminishing. Approximating with the mean Fourier coefficient, as a_{kD} does, will significantly over estimate the effect of wire drag variation for large wavelengths. The combined wake equation will over predict the wake strength at large $\overline{x}$. For the $\beta = 50\%$, the Fourier coefficients for small k increase with σ_δ. Only for the $\sigma_\delta = 0.75$ zither are the Fourier coefficients spread relatively evenly across the spectrum, meaning σ_a should be an accurate representation. The wake decay should reduce from $x^{-0.75}$ at large streamwise distances. Indeed, figure 5 does show the wake decay reducing for this zither.

The Fourier coefficients of the $\beta = 40\%$ zither show the largest increase at wavenumbers $k > 200$, raising σ_a but not affecting the far wake. A wavenumber of $k = 288$ corresponds to a wavelength of approximately $2M$, i.e. a wavelength that could be expected to be associated with the coalescence of adjacent jets.

The failure of the combined wake strength equation (2.25) is attributed to the assumed Fourier coefficient distribution due to variation in wire source strength (drag), a_{kD} for most zithers. Approximating the Fourier coefficients due to wire force variation as constant independent of k is not valid and leads to over prediction of the wake strength at large $\overline{x}$. Equations to predict wake strength more accurately require a understand-

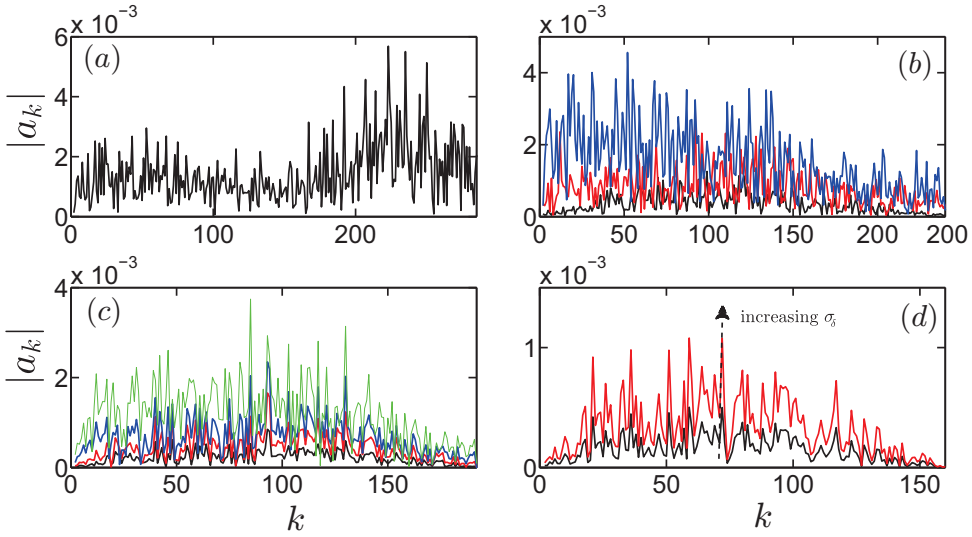

FIGURE 8. Fourier coefficients at the zither due to variation in drag only, calculated with (2.28): (*a*) $\beta = 40\%$; (*b*) $\beta = 50\%$; (*c*) $\beta = 60\%$; (*d*) $\beta = 66.67\%$. Increasing coefficients is increasing σ_δ. Lines: —— $\sigma_\delta = 0.025$; —— $\sigma_\delta = 0.05$; —— $\sigma_\delta = 0.075$; —— $\sigma_\delta = 0.1$. (colour online)

ing of how the drag of a wire varies with an error in its position, particularly at low wavenumbers.

2.11. *Wake wavelength*

Equation (2.21) predicts the dominant wake wavelength should increase with $\overline{x}^{0.5}$ and be independent of the zither geometry. As σ_a is small and over predicts the effect of low wavenumbers for the current zithers, it is expected (2.21) should be valid. The largest amplitude Fourier mode is extracted from the CFD simulations via an FFT on spanwise velocity profiles and shown in figure 9. Agreement with (2.21) is good and the wake wavelength does appear to be independent of the zither geometry. Wake profiles can also be calculated from knowledge of the individual wire source strength and position data (see Pook 2013).

2.12. *Coalescence of jets*

Figures 10 and 11 show contours of streamwise velocity for a limited extent ($< 10\%$) of the $\beta = 40\%$, 50% and 60% zithers. The $\beta = 60\%$ zithers share the same wire perturbation pattern. Apart from the longer jets and wakes, the flow pattern does not significantly change over the σ_δ range investigated. There is minimal deflection of the jets that is taken to indicate the coalescence of jets in experimental flow visualisation and table 1 shows the ratio of σ_a/σ_δ is near constant. For the $\beta = 50\%$ zither with $\sigma_\delta = 0.075$ zither shown in figure 11(*c*), the jets emanating near the cylinder at at $z/d \approx 135$ are visibly deflected away from each other, creating an extended region of low speed flow. More instances of visible jet deflection can be observed for this zither, and particularly the $\beta = 40\%$ zither, but not the other zithers. The ratio σ_a/σ_δ increases for zithers with instances of jet deflection.

The jet deflection pattern is similar to the experimental visualisations of Le Gal *et al.* (1996) where extended void regions were observed but significant deflection was observed for the majority of jets. As previously mentioned, the Fourier coefficients of the $\beta = 40\%$ zither increase rapidly for $k > 200$. This indicates a flow pattern that possibly correlates

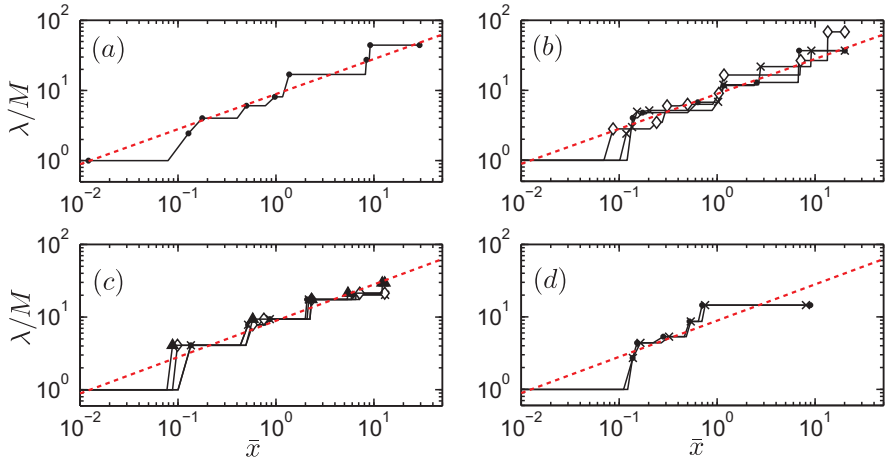

FIGURE 9. Wavelength of the peak Fourier mode in the CFD simulation; (*a*) $\beta = 40\%$; (*b*) $\beta = 50\%$; (*c*) $\beta = 60\%$; (*d*) $\beta = 66.67\%$. Lines: ----- Wavelength predicted by (2.21) (colour online); Marked lines as for figure (5).

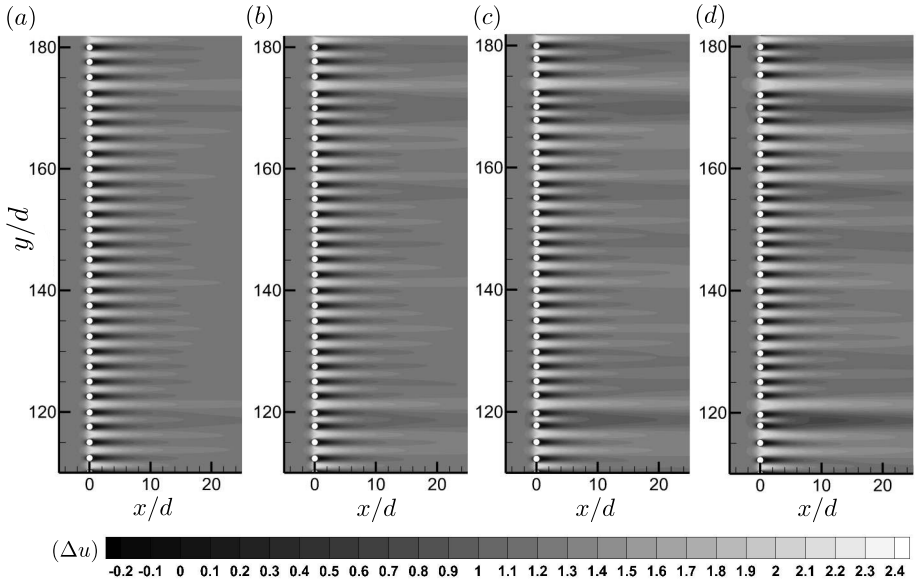

FIGURE 10. Contours of streamwise velocity scaled by free-stream velocity U (see insert for scale) for a limited extent (<10%) of the zithers, $\beta = 60\%$ with: (*a*) $\sigma_\delta = 0.025$; (*b*) $\sigma_\delta = 0.05$; (*c*) $\sigma_\delta = 0.075$; (*d*) $\sigma_\delta = 0.1$.

to the coalescence of jets. However, such small wavelengths have no effect on the far wake strength. For all other zithers, there is no trend for increased drag variation at wavelengths approaching $2M$. The authors opinion is that the coalescence of jet phenomena appears only sporadically in the zither simulations, based on a comparison to the Bradshaw (1965) and Le Gal *et al.* (1996) visualisations.

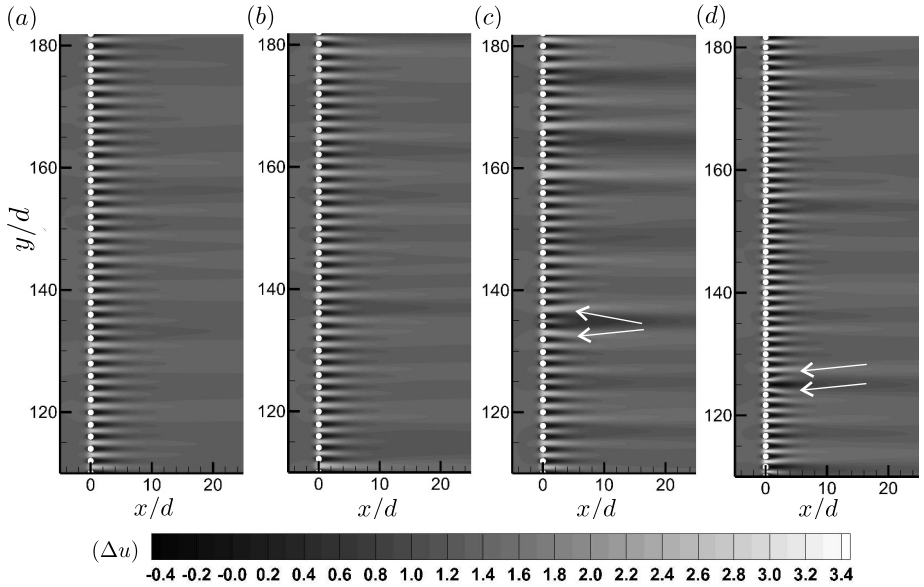

FIGURE 11. Contours of streamwise velocity scaled by free-stream velocity U (see insert for scale) for limited extent (<10%) of the zithers: (*a*) $\beta = 50\%$ with$\sigma_\delta = 0.025$; (*b*) $\beta = 50\%$ with $\sigma_\delta = 0.05$; (*c*) $\beta = 50\%$ with $\sigma_\delta = 0.075$; (*d*) $\beta = 40\%$ with $\sigma_\delta = 0.025$.

2.13. *The effect of non-uniform inflow*

A non-uniform inflow may force the $\overline{x}^{-0.25}$ wake decay rate. Limited CFD simulations are performed with a random inlet velocity wake (U_r) constructed by the addition of sinusoids, from $k = 1$ to 50, each with an amplitude of $0.002U$ and random phase,

$$U_r = U + \sum_{k=1}^{50} 0.002U \sin\left(\frac{2\pi k}{960}\frac{z}{d} + \text{random phase}\right). \tag{2.36}$$

The mean strength of the inlet velocity is $\Delta u = 1\%$ and its profile is shown in figure 12(*a*). The non-uniform inflow is applied to the $\beta = 40\%$, 50% and 60% zithers with σ_δ=0.025. The $\beta = 40\%$ and 50% zithers streamwise domain is extended to ensure any change of wake decay is captured.

Contours of velocity near the zither (not shown) are not discernibly different from the uniform inflow simulations. The wake strength is shown in figure 12(*b*). For small $\overline{x}$, there is little difference compared to a uniform inflow, but far downstream the wake decay changes from $\bar{x}^{-0.75}$ towards $\bar{x}^{-0.25}$. This is more readily apparent for the $\beta = 60\%$ zither.

At $\overline{x} = 10$, the wake of the $\beta = 60\%$ zither has been increased by 50% relative to a uniform inflow. The $\beta = 50\%$ zither wake is 16% greater and the $\beta = 40\%$ zither is only 9% greater. The standard deviations of wire source strength (σ_a) for the $\beta = 40\%$, 50% and $\beta = 60\%$ zithers are 0.0093, 0.0045 and 0.0058 respectively. As σ_δ is the same, the combined wake strength equation 2.25 would predict the $\beta = 40\%$ zither wake to show a greater deviation from $\overline{x}^{-0.75}$ decay, opposite to what is observed in figure 12(*b*).

The Fourier coefficients at $\overline{x} = 10$ are extracted from the CFD simulations and shown in figure 12(*c–e*). Also shown are the Fourier coefficients for the uniform inflow simulations, and the Fourier coefficients calculated from the individual wire drag and position data (2.9) and scaled by (2.5). With a non-uniform inflow, the Fourier coefficients extracted

from the simulation at low wavenumbers are significantly smaller than calculated. This increases the calculated value of σ_a relative to that observed. The difference can be explained by considering the non-uniform inflow contribution to the initial condition. Assuming the non-uniform inflow can be added linearly to the wire wakes, then the Fourier coefficients at the zither are,

$$a_k = \frac{\overline{q}}{L} \sum_{n=1}^{N} \left(-2\pi i K \delta_n + a_n - 2\pi i K a_n \delta_n\right) \exp\left(-2\pi i K n\right) - a_{kw}, \tag{2.37}$$

where a_{kw} is the k^{th} Fourier coefficient of the non-uniform inflow at the zither assuming no influence of the zither. It is subtracted due to the convention of a wake being positive.

Figure 12 reveals the addition of the inflow term, known as the input wake is defined, produces good agreement between the downstream calculated and simulation Fourier coefficients. The reduced sensitivity to non-uniform inflow with decreasing open-area ratio can be partly explained by noting that the mean source strength increases rapidly with decreasing open-area ratio while the inflow contribution is constant. Thus, the relative influence of the non-uniform inflow reduces. Figure 12 shows that with decreasing open-area ratio, the change in wire drag Fourier coefficients induced by the non-uniform inflow tends towards the equal and opposite value of the non-uniform profile Fourier coefficient, i.e. the drag variation induced across the zither will cancel out the non-uniform inflow leaving a wake due to the imperfect wire position and the variation of drag this induces. Hence, the far wake strength of the lower-open area ratio zithers with a non-uniform inflows differs less compared to a uniform inflow. The removal of a non-uniform inflow with increasing screen pressure drops (increasing $\bar{q}$) is predicted in the Taylor & Batchelor (1949) analysis.

The non-uniform inflow results demonstrate the far wake strength of an imperfect zither can be increased substantially by a non-uniform inflow, particularly as open-area ratio increases. For the zithers examined, the $\beta = 60\%$ zither far wake becomes stronger than that of the $\beta = 50\%$ zither.

3. Zither wakes through the contraction

The zither wakes of normal vorticity pass through a contraction on the way to the test-section. A moderate contraction will remove a majority of the Δu wake component, yet increased spanwise variation of the test-section layer is often reported in literature reported when poor quality screens are used upstream of a contraction. Pook & Watmuff (2014) demonstrated the ability of a contraction to tilt and stretch normal vorticity into streamwise vorticity at the exit. Using the same 5:1, two-dimensional contraction with length $L_c = 1524$ mm and test-section geometry as the current study, they showed the maximum streamwise vorticity (ω_x) at the test-section leading edge was 60% of the normal vorticity (ω_y) entering the contraction.

The uniform inflow zither wakes are sampled $197d$ downstream of the zither and imposed $957d$ upstream of the contraction start. Due to symmetry, only the lower-half of the contraction is modelled. The contraction mesh uses structured, near orthogonal CV, with 440, 200 and 500 CV in the streamwise, wall-normal and spanwise directions respectively. Pook & Watmuff (2014) demonstrated this mesh resolution accurately reproduced the wake of a single wire passing through a contraction by comparison to the experimental observations of Watmuff (2006).

Figure 13 provides an example of a two-dimensional zither wake entering the contraction and contours of the streamwise vorticity on a plane $394d$ downstream of the exit.

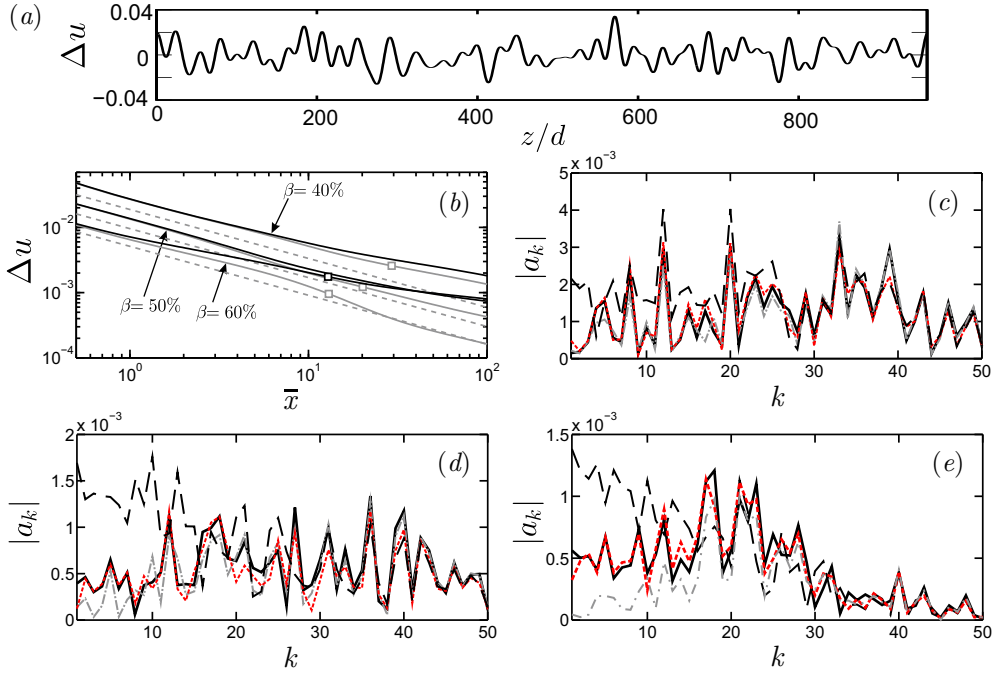

FIGURE 12. (*a*) Non-uniform velocity inlet profile. (*b*) Wake strength, $\beta = 40\%$, 50%, 60% with $\sigma_\delta = 0.025$ zithers. Dark solid line (stronger wake) is non-uniform inflow. Light solid line is uniform inflow. Square makers indicated strength downstream calculated with (2.2). Dashed lines are (2.27). (*c*) Fourier coefficients at $\overline{x} = 10$ for $\beta = 40\%$. (*d*) Fourier coefficients at $\overline{x} = 10$ for $\beta = 50\%$. (*e*) Fourier coefficients at $\overline{x} = 10$ for $\beta = 60\%$. Lines: —— Extracted from CFD with non-uniform inflow; -·- Extracted from CFD with uniform inflow; ----- Calculated with (2.13) and (2.5); ····· Calculated with (2.37) and (2.5). (colour online)

The streamwise vorticity exiting has been scaled by the standard deviation of the normal vorticity entering the contraction ($\sigma_{\omega y\, in}$). On the downstream plane, the contraction floor is located at $y/d = 0$. The leading edge to be used in the §4 is located at $y = 186d$.

The stronger regions of streamwise vorticity near the contraction floor boundary is due to the combination of Görtler instability near the no-slip contraction wall, and the tilting and stretching mechanism as discussed by Pook & Watmuff (2014). The spanwise pattern of streamwise vorticity is consistent with distance above the contraction boundary layer. The apparent wake wavelength changes little through the contraction. The magnitude of the streamwise vorticity reduces to zero at the contraction centreline.

The streamwise vorticity on a spanwise profile downstream of the contraction exit, at the height of the leading edge is shown in figure 14. The strongest streamwise vorticity is seen for the $\beta = 50\%$ with $\sigma_\delta = 0.075$ zither. The maximum streamwise velocity on a spanwise profile 11 leading edge half-thicknesses (h) upstream of the leading edge is less than 0.2% of U (not shown). The v component of the wake is strongest and reaches nearly 0.5% of the free-stream velocity, giving a flow angle of 0.26 degrees. However, the standard deviation of the v component flow angle is only 0.1° and is a better indicator of what would be measured by a survey of flow quality. More details can be found in Pook (2013).

An FFT on the spanwise profile of streamwise vorticity is shown in figure 15. The peak wavenumber occurs at $k = 10$ to 12 for all zithers, except the $\beta = 66.67\%$ zithers which have peaks to $k = 21$. As expected, smaller wavelengths have decayed.

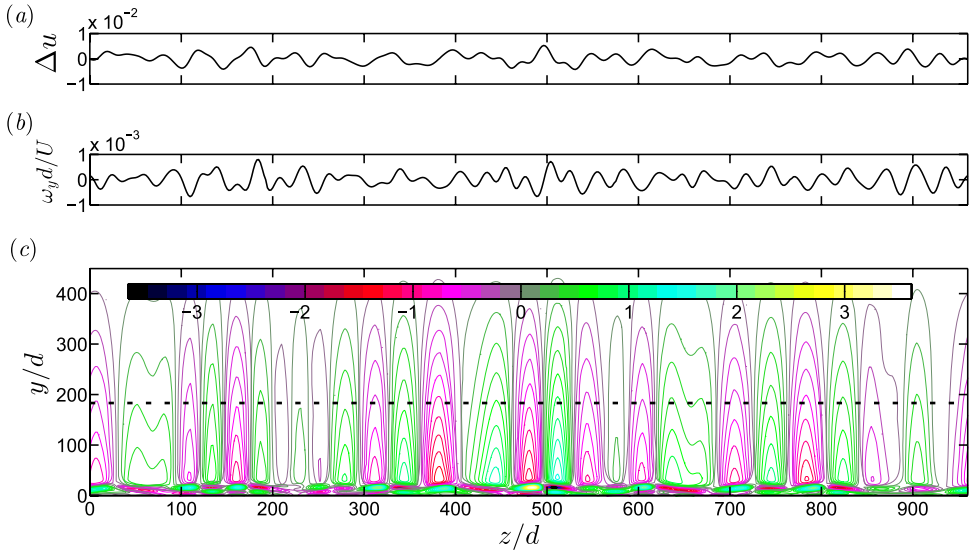

FIGURE 13. Wake of the $\beta = 50\%$ with $\sigma_\delta = 0.025$ zither entering the contraction and streamwise vorticity out. (a) Wake spanwise profile of Δu entering contraction. (a) Wake spanwise profile of normal vorticity (ω_y) entering contraction. c) Contours of streamwise vorticity ($\omega_x/\sigma_{\omega y\,in}$), $394d$ downstream of the contraction exit. Dashed line is leading edge of §4. (colour online)

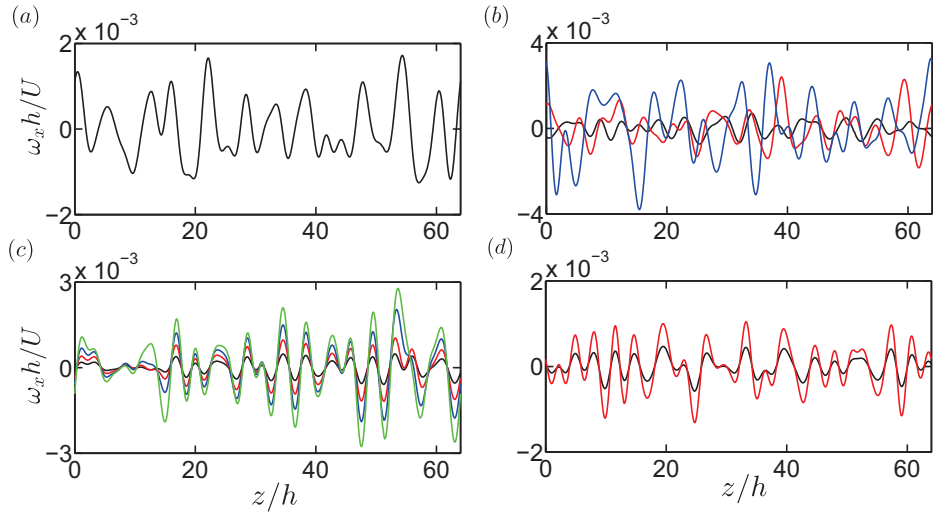

FIGURE 14. Streamwise vorticity $394d$ downstream of the contraction exit, $186d$ above the contraction floor: (a) $\beta = 40\%$; (b) $\beta = 50\%$; (c) $\beta = 60\%$; (d) $\beta = 66.67\%$. Increasing ω_x is increasing σ_δ. Lines: —— $\sigma_\delta = 0.025$; —— $\sigma_\delta = 0.05$; —— $\sigma_\delta = 0.075$; —— $\sigma_\delta = 0.1$. (colour online)

Table 2 lists the standard deviation of the normal vorticity entering the contraction ($\sigma_{\omega y\,in}$), and the standard deviation of the streamwise vorticity measured on the spanwise profile after the contraction at the height of the leading edge to be used in the §4, ($\sigma_{\omega x\,out}$). The ratio varies between 0.30 and 0.45, increasing with a decrease in screen open-area ratio and increase in σ_δ. For a given zither spacing M ($\overline{x}$ is the same), the vorticity ratio would be expected to remain a constant. However, differing wake decay rates due to relatively stronger large wavelengths could modify this ratio.

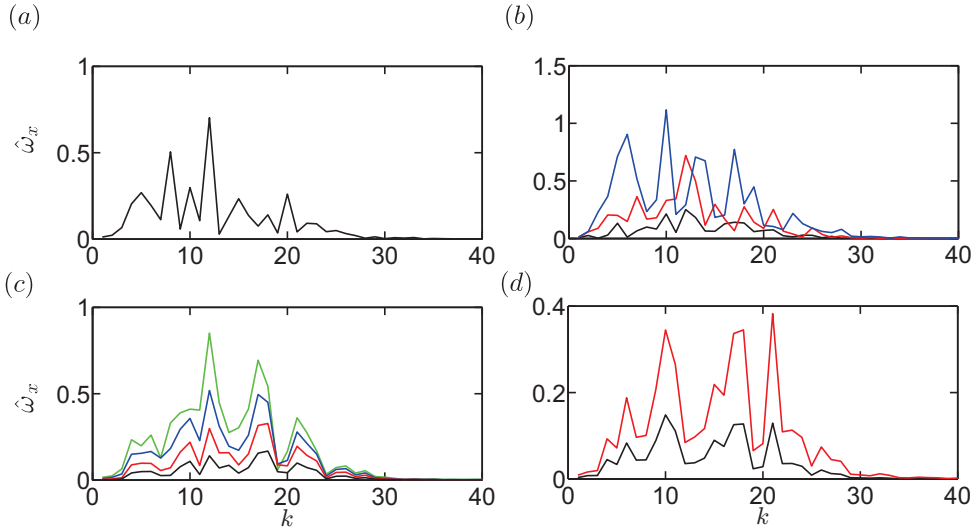

FIGURE 15. Streamwise vorticity FFT ($\hat{\omega}_x$) 394d downstream of the contraction exit, 186d above the contraction floor, vorticity is dimensional (s^{-1}): (a) $\beta = 40\%$; (b) $\beta = 50\%$; (c) $\beta = 60\%$; (d) $\beta = 66.67\%$. Increasing $\hat{\omega}_x$ is increasing σ_δ. Lines: —— $\sigma_\delta = 0.025$; —— $\sigma_\delta = 0.05$; —— $\sigma_\delta = 0.075$; —— $\sigma_\delta = 0.1$. (colour online)

β %	σ_δ	$\sigma_{\Delta u\, in}$ %	$\sigma_{\omega y\, in}$ (s^{-1})	$\sigma_{\omega x\, out}$ (s^{-1})	$\sigma_{\omega x\, out}/\sigma_{\omega y\, in}$
40.00	0.025	0.41	3.62	1.57	0.43
50.00	0.025	0.20	1.90	0.73	0.38
50.00	0.050	0.46	4.04	1.81	0.45
50.00	0.075	0.88	7.56	3.28	0.43
60.00	0.025	0.19	1.78	0.54	0.30
60.00	0.050	0.37	3.53	1.08	0.31
60.00	0.075	0.55	5.16	1.75	0.34
60.00	0.100	0.74	6.72	2.49	0.37
66.67	0.025	0.17	1.65	0.51	0.31
66.67	0.050	0.36	4.03	1.31	0.32

TABLE 2. Ratio of $\sigma_{\omega x\, out}$ on a profile 394d downstream of contraction exit and, 186d above contraction floor, to $\sigma_{\omega y\, in}$.

The zither wake decay through the contraction is examined with the ratio,

$$\Delta u_c = \frac{\Delta u_{local}}{\Delta u_0}, \tag{3.1}$$

where, Δu_c is the wake strength on the contraction centreline normalised by the local velocity on the contraction centreline, and scaled by the wake strength at the contraction entry (Δu_0), i.e. the zither wake strength. Figure 16 plots the scaling. Decreasing zither open-area ratio and increasing σ_δ creates a stronger wake out of the contraction. This can be attributed to the large wavelength modes (small k) being relatively larger for these zither wakes. The trend in figure 16 holds across a contraction cross-section. The variation of Δu_c at the contraction exit for the uniform inflow zither wakes varies by a factor of 2 .

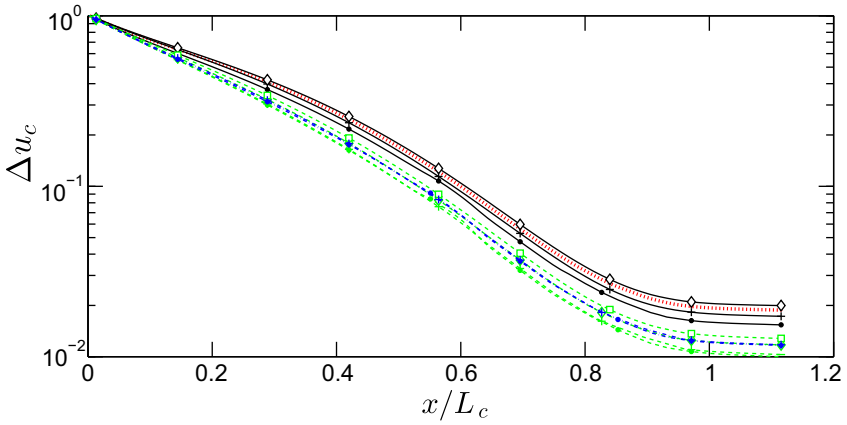

FIGURE 16. Scaled wake strength on the contraction centreline, Δu_{cont} defined by (3.1). The contraction curvature begins at $x/L_c = 0$ and ends at $x/L_c = 1$, $L_c = 1.524$m. Lines: $\beta = 40\%$ $\sigma_\delta = 0.025$; $\beta = 50\%$ $\sigma_\delta = 0.025$; $\beta = 50\%$ $\sigma_\delta = 0.05$; $\beta = 50\%$ $\sigma_\delta = 0.075$; $\beta = 60\%$ $\sigma_\delta = 0.025$; $\beta = 60\%$ $\sigma_\delta = 0.05$; $\beta = 60\%$ $\sigma_\delta = 0.075$; $\beta = 60\%$ $\sigma_\delta = 0.1$; $\beta = 66\%$ $\sigma_\delta = 0.025$. (colour online)

4. Test-section flat-plate boundary layer

The streamwise vorticity in the flow past the test-section leading edge create streaks in the boundary layer. Receptivity to low frequency streamwise vorticity has been shown by Schrader *et al.* (2010) to be a dominant mechanism. The same leading edge geometry as Pook & Watmuff (2014) with a slot mass-flow of 0.21 is used (see Pook & Watmuff (2014) for details). Blasius flow is achieved by $R = 400$ where,

$$R = \sqrt{\frac{Ux}{\nu}}, \tag{4.1}$$

as indicated by the shape factor in figure 17. The virtual origin is small and of little consequence to the results to be presented. Shifting the attachment point has minimal affect on the receptivity to streamwise vorticity (Pook & Watmuff 2014). The free-stream velocity over the flat-plate region is $U = 8.6$ ms^{-1}.

The mesh in the test-section boundary layer is highly orthogonal with approximately 40 CV in the wall-normal direction and 500 CV in the spanwise direction. The total mesh size is approximately 45 million CV. This is a similar level of refinement as Mesh$_2$ in Pook & Watmuff (2014) that was shown by a grid refinement study to accurately calculate the streak strength.

4.1. *Measures of Streak Strength*

Various measures of streak strength have been favoured in literature with no direct relations provided between them. Figure 18 documents streak strength ($\Delta\delta^*$) as measured by the maximum and minimum displacement thickness on a given cross-sectional plane,

$$\Delta\delta^* = \frac{\max(\delta^*) - \min(\delta^*)}{\delta^*_{base}}, \tag{4.2}$$

where the subscript *base* indicates the two-dimensional flow with no streaks. Figure 18 shows the corresponding streak amplitude (A) defined by,

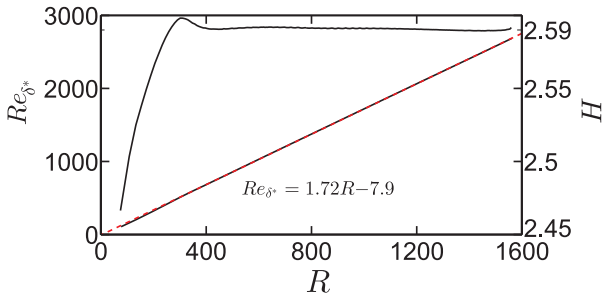

FIGURE 17. Two-dimensional base-flow. Reynolds number based on displacement thickness (Re_{δ^*}) versus R and shape factor (H) versus R. Perfect Blasius displacement thickness growth shown with -----. Equation is fit to CFD data. The leading edge ends and the flat-plate begins at $R = 345$.

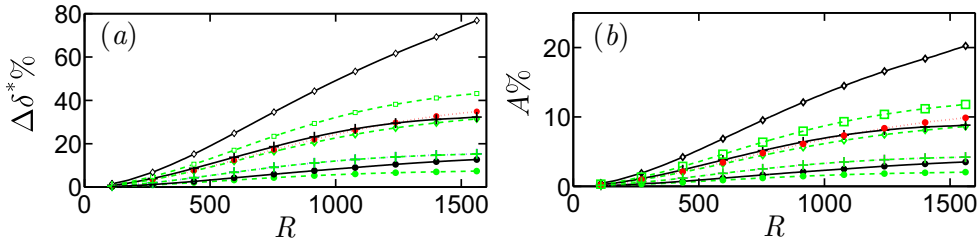

FIGURE 18. (a) Streak strength $\Delta\delta^*$ versus R. (b) Streak amplitude (A) versus R. Lines and markers as for figure 16. (colour online)

$$A = \frac{\max\left[U\left(y,z\right) - U_{base}\left(y\right)\right] - \min\left[U\left(y,z\right) - U_{base}\left(y\right)\right]}{2U}. \tag{4.3}$$

Both measures are linear with $x^{0.5}$, downstream of an initial receptivity region, until $R \approx 1000$.

The ratio of $\Delta\delta^*$ to A beyond $R > 400$ is approximately 3.6 for all zithers except the $\beta = 40\%$ with $\sigma_\delta = 0.075$ and $\beta = 50\%$ with $\sigma_\delta = 0.075$ zithers. For these zithers, the ratio varies between between 3.5 to 3.8 with increasing R. These zithers have larger amplitude Fourier modes at low wavenumbers. The optimal non-modal growth theory of Andersson *et al.* (1999) and Luchini (2000) explains that larger spanwise wavelength disturbances will exhibit greater growth and peak further downstream. Indeed, the $\beta = 50\%$ with $\sigma_\delta = 0.075$ zither generates the largest streak growth by a substantial margin with a peak beyond the streamwise domain ($R > 1600$). The growth of the weaker zither streaks can be seen to be slowing towards the end of the streamwise domain.

The streak growth qualitatively agrees with the compiled Klebanoff streak data of Westin *et al.* (1994) which shows linear growth with $x^{0.5}$. Only three data-sets extend beyond $R = 1500$ with one set showing a peak and then decrease downstream while the other two show a rapid increase which probably indicates transition. It should be noted that experimental measures of Klebanoff streaks are u_{rms} and not directly the streak amplitude measured here.

Streak strength and amplitude as defined are measures of minimum and maximum deviation from the two-dimensional layer. The standard deviation of these quantities for steady streaks is likely to have a closer relation to the experimental measures of unsteady streaks (e.g. u_{rms}) and any possible correlation with TS suppression. The standard devi-

ation of streak strength and amplitude are shown in figures 19. The standard deviation of streak strength ($\sigma_{\Delta\delta^*}$) at a given streamwise plane is defined by,

$$\sigma_{\Delta\delta^*} = \frac{1}{\delta^*_{base}}\sqrt{\frac{1}{L}\int_0^L \delta^{*2} dz}, \tag{4.4}$$

and the standard deviation of streak amplitude (σ_A) by,

$$\sigma_A = \sqrt{\frac{1}{U^2 L}\int_0^L \max\left[\left(U\left(y\right) - U_{base}\left(y\right)\right)^2\right] dz}, \tag{4.5}$$

where the subscript *base* indicates the two-dimensional layer without streaks. The standard deviation measures are significantly less than the maximal measures but the same relative trends are observed.

Skin-friction also provides a measure of streak growth. Figure 19 shows the variation in skin friction defined by,

$$\sigma_{c_f} = \frac{2\nu}{U^2}\sqrt{\frac{1}{L}\int_0^L \left(\frac{\partial U}{\partial y} - \overline{\frac{\partial U}{\partial y}}\right)^2 dz}, \quad \overline{c_f} = \frac{2\nu}{U^2}\overline{\frac{\partial U}{\partial y}}, \quad \overline{\frac{\partial U}{\partial y}} = \frac{1}{L}\int_0^L \frac{\partial U}{\partial y} dz \tag{4.6}$$

$$\Delta c_f = \frac{\sigma_{c_f}}{\overline{c_f}}, \tag{4.7}$$

where Δc_f is the ratio of skin-friction standard deviation to the mean value, and the wall-normal velocity gradients are measured at the wall. The ratio of Δc_f to σ_A is not constant and varies between 1.65 and 1.9 for the current zither streaks. Skin friction variation between 1.5% and 18% at $R = 1550$, an order of magnitude variation. Bradshaw (1965) measured turbulent skin friction variation exceeding 10% when screens with $\beta < 57\%$ were installed in the settling chamber. Only the $\beta = 50\%$ with $\sigma_\delta = 0.075$ zither exceeds 10% for the current results.

Based on the magnitude of skin friction variation for the $\beta = 50\%$ with $\sigma_\delta = 0.075$ zither, it seems likely that the cause of the spanwise variation in the results of Bradshaw (1965) is present in the current simulations. Bradshaw (1965) attributed the variation to a spatial "instability" downstream of the screen leading to the coalescence of jets. The current simulations suggest the cause can be interpreted as being due to the variation of wire drag and wire position across the zither.

4.2. *Streak amplitude related to the zither*

Ideally, a simple relation can be found to relate streak amplitude to the zither geometry. Relating streak growth to a single measure of velocity variation in the wake will fail as streak growth is strongly dependent on spanwise wavelength. The relation must be made in terms of vorticity and consider the spectral distribution. However, the current zithers wakes do share a similar spanwise wavelength as the zither position is constant and the zither wake wavelength formula was found to be accurate (see figure 9). The contraction and leading edge geometry are also identical. Thus, the streak amplitude can be scaled by the wake strength entering the contraction. If all zither wakes maintain the same wake decay rate, and the streak growth in the test-section layer is linear with amplitude, then a measure of streak amplitude scaled by a measure of the zither wake entering the contraction should collapse to a single curve. Figure 19(d) shows the standard deviation

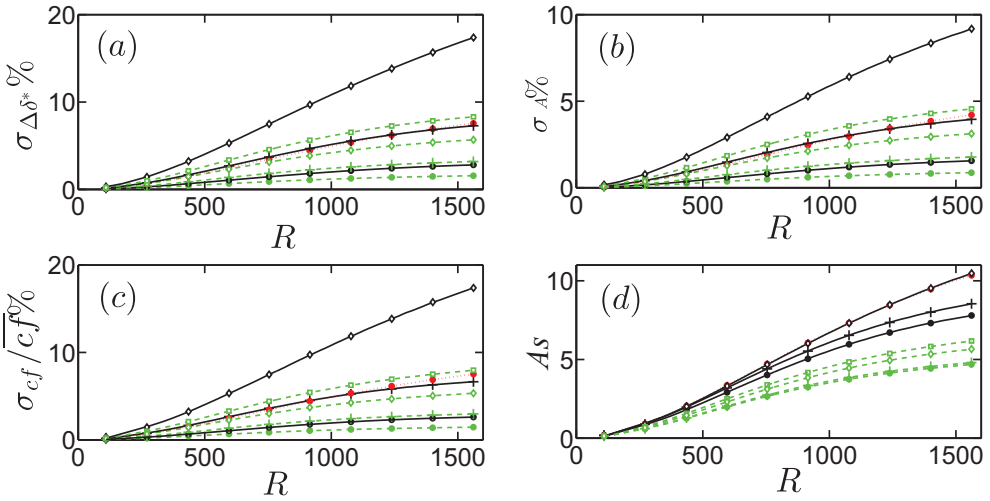

FIGURE 19. (*a*) Standard deviation of streak strength $\sigma_{\Delta\delta^*}$ versus R. (*b*) Standard deviation of streak amplitude σ_A versus R. (*c*) Standard deviation of normalised skin-friction $\sigma_{cf}/\overline{cf}$ versus R. (*d*) Streak strength scaled to zither wake before contraction (As) versus R. Lines and markers as for figure 16. (colour online)

of streak amplitude (σ_A) scaled by the standard deviation of the zither wake strength entering the contraction ($\sigma_{\Delta u/U\,in}$),

$$As = \frac{\sigma_A}{\sigma_{\Delta u/U\,in}} \tag{4.8}$$

The $\beta = 66.67\%$ and $\beta = 60\%$ zithers with $\sigma_\delta = 0.025$ and $\sigma_\delta = 0.05$ streak growth collapses with this scaling. However, the $\beta = 60\%$ zithers with $\sigma_\delta = 0.075$ and $\sigma_\delta =$ 0.1show an increased scaled streak growth. This indicates a stronger wake, due to a reduced wake decay rate far downstream of the zither. Decreasing β for a given σ_δ also increases the scaled streak growth. This is highlighted by the $\beta = 40\%$ with $\sigma_\delta = 0.025$ and $\beta = 50\%$ with $\sigma_\delta = 0.075$ zithers that have nearly identical scaled streak growth. Their scaled streak amplitude is more than double that for the $\beta = 66.67\%$ with $\sigma_\delta = 0.05$ zither at $R = 1500$. Although the dominant Fourier mode in the wake is of a similar wavelength, the spectral distribution is not. Figure 15 shows they have larger amplitude Fourier coefficients below $k = 10$, creating larger streaks further downstream. A simple relation between the zither and the streak amplitude cannot be found.

4.3. *Spanwise mean quantities*

Figure 20(*a*) Spanwise mean shape factor (H) versus R. shows the zither streaks have a negligible affect on the spanwise mean displacement thickness, consistent with experimental observations of Klebanoff streaks (Westin *et al.* 1994). However, figure 20(*b*) reveals the mean shape factor decreases with streamwise distance relative to the two-dimensional layer. Stronger streaks produce a greater decrease. Westin *et al.* (1994) reported a decreasing shape-factor when FST induced Klebanoff streaks are present, observing a shape factor of 2.41 at $R = 1260$. Only the $\beta = 50\%$ with $\sigma_\delta = 0.075$ zither produces a comparable mean shape factor but it occurs further downstream.

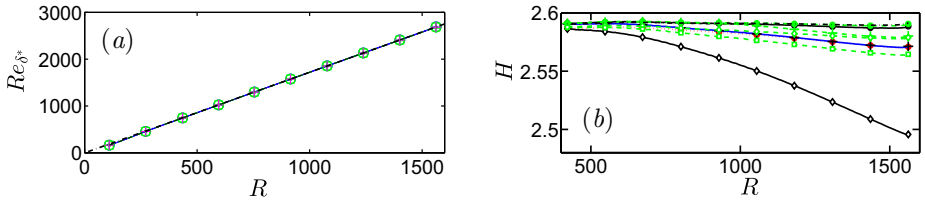

FIGURE 20. (*b*) Spanwise mean displacement thickness versus R. (*b*) Spanwise mean shape factor (H) versus R. -·-·- Two-dimensional base-flow. Other lines and markers as for figure 16 (colour online)

4.4. *Streak wall-normal velocity profiles*

The presence of streaks causes a deviation in the velocity profile relative to the undisturbed two-dimensional base-flow. The deviation is defined by,

$$\frac{\Delta U}{U_e} = \frac{U\left(y\right) - U_{base}\left(y\right)}{U_e}, \tag{4.9}$$

where U_e is the edge velocity of the layer. Kendall (1985; 1998) measured time-averaged velocity profiles in the presence of Klebanoff streaks to be in decrement across the entire layer ($\Delta U/U_e$<0). The largest decrement occurring at approximately $\eta = 3$. Westin *et al.* (1994) observed the time-averaged profiles to be in excess near the wall and decrement in the outer layer, an "s" shape. The maxima (lower part of "s") was slightly greater than the minima (upper part of "s"). This led to a reduction in the measured shape factor downstream as was found for the spanwise means of the current zither wake streaks (see figure 20).

Figure 21 plots the streamwise velocity deviation relative to the undisturbed two-dimensional layer at $R = 1350$ for the zither wakes. For the majority of the zither streak flows, the spanwise average shows an excess near the wall and a larger maximum decrement higher in the layer, in agreement with Westin *et al.* (1994). However, the velocity is in excess across the layer for the weakest zither streaks, $\beta = 60\%$ with $\sigma_\delta = 0.025$ and $\sigma_\delta = 0.05$. The $\beta = 60\%$ zithers share the same wire perturbation pattern. At $R = 500$ for weak streaks, a very small decrement can be seen across the layer as observed by Kendall (1985) whom measured at $R = 980$. However this trend does not exist in the current data at $R = 1000$.

With increasing σ_δ, the spanwise mean deviation for the $\beta = 60\%$ zithers develops the "s" shape. This suggests the strength of the streaks is responsible. The maximum decrement in the Kendall (1998) data is 0.02 while the Westin *et al.* (1994) data is 0.06, reinforcing this suggestion, although spanwise scales may be a factor. The cause of the excess compared to the decrement as measured by Kendall (1985) and Kendall (1998) is uncertain.

The peak of the excess deviation (lower curve of the "s") can be seen in figure 21 to shift lower in the layer with increasing amplitude. The opposite occurs for the velocity decrement higher in the layer (upper curve of the "s"). This behaviour agrees with the simulations by Jacobs & Durbin (2001) where backwards jets (unsteady streaks) were observed to lift towards the boundary layer edge prior to breakdown. The PIV of Nolan & Walsh (2012) also observed the peak excess to move towards the wall while the low-speed streak moves away from the wall.

4.5. *Streak Fourier mode energy*

An FFT is used to decompose the zither streaks,

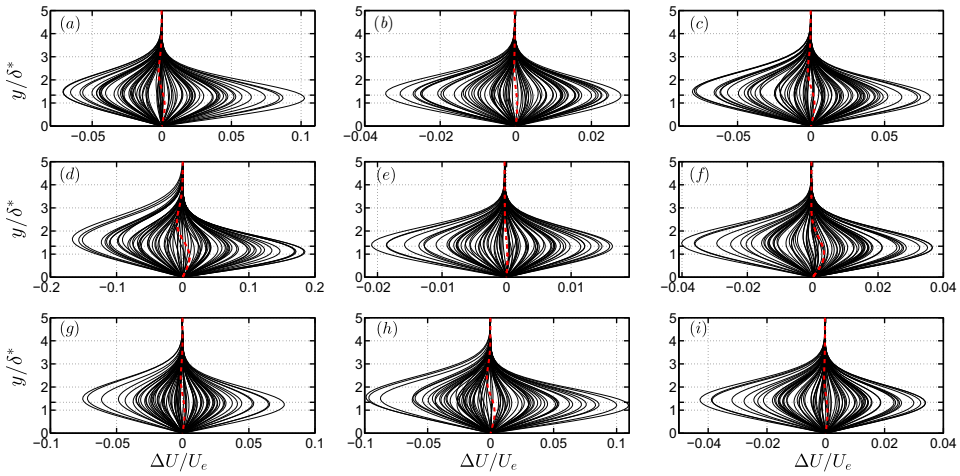

FIGURE 21. Wall-normal profiles of $\Delta U/U_e$, defined by (4.9), at various spanwise positions and $R = 1350$. Lines: —— $\Delta U/U_e$ at some spanwise position; ----- Spanwise mean $\Delta U/U_e$. (*a*) $\beta = 40\%$ $\sigma_\delta = 0.025$; (*b*) $\beta = 50\%$ $\sigma_\delta = 0.025$; (*c*) $\beta = 50\%$ $\sigma_\delta = 0.05$; (*d*) $\beta = 50\%$ $\sigma_\delta = 0.075$; (*e*) $\beta = 60\%$ $\sigma_\delta = 0.025$; (*f*) $\beta = 60\%$ $\sigma_\delta = 0.05$; (*g*) $\beta = 60\%$ $\sigma_\delta = 0.075$; (*h*)$\beta = 60\%$ $\sigma_\delta = 0.1$; (*i*) $\beta = 66\%$ $\sigma_\delta = 0.025$. (colour online)

$$Q = \sum_{k=-\infty}^{\infty} \hat{Q}\,(x, y) \exp\left(ik\beta z\right), \tag{4.10}$$

where $Q\,(x, y, z) = [U, V, W]^T$, k is an integer wavenumber and β is the fundamental wavenumber of the domain of width L,

$$\beta = \frac{2\pi}{L}. \tag{4.11}$$

The energy of a given mode k at a given streamwise position is found as,

$$\hat{E}^k = \int_0^{6\delta^*} \left(\hat{U}^k\right)^2 + \left(\hat{V}^k\right)^2 + \left(\hat{W}^k\right)^2 dy, \tag{4.12}$$

where the choice of the limit $6\delta^*$ is arbitrary. The energy is scaled by the energy of the same Fourier mode in the free-stream wake, sampled on a spanwise velocity profile 63.5mm upstream of the leading edge ($\hat{E}'_{ref}$), and the Reynolds number when $\beta\delta = 0.45$ for the given mode ($Re_{0.45}$) where,

$$\delta = \sqrt{\frac{\nu x}{U}}. \tag{4.13}$$

A non-dimensional streamwise coordinate can be defined as,

$$\overline{X} = \left(\frac{\beta\delta}{\beta_{0.74}}\right)^2, \tag{4.14}$$

where $\beta_{0.74}$ is set to 0.74 so that the linear Optimal streak would reach a maximum energy at $\overline{X} = 1$ (Andersson *et al.* 1999). This allows mode growth to be compared with the Optimal streak as done by Fransson *et al.* (2004).

The streamwise energy development of the modes $k = 10$ and 15 energy is shown in

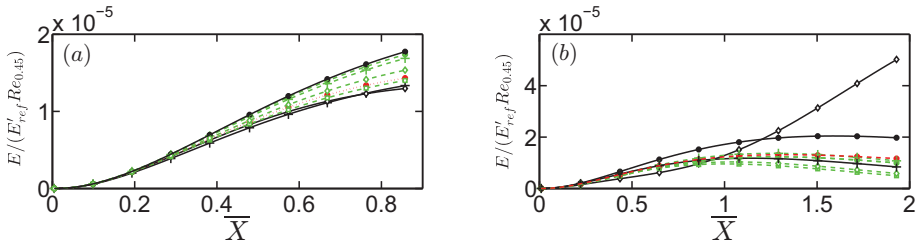

FIGURE 22. Mode energy versus non-dimensionalised streamwise distance ($\overline{X}$) for the Fourier mode: (a) $k = 10$; (b) $k = 15$. Lines and markers as for figure 16. (colour online)

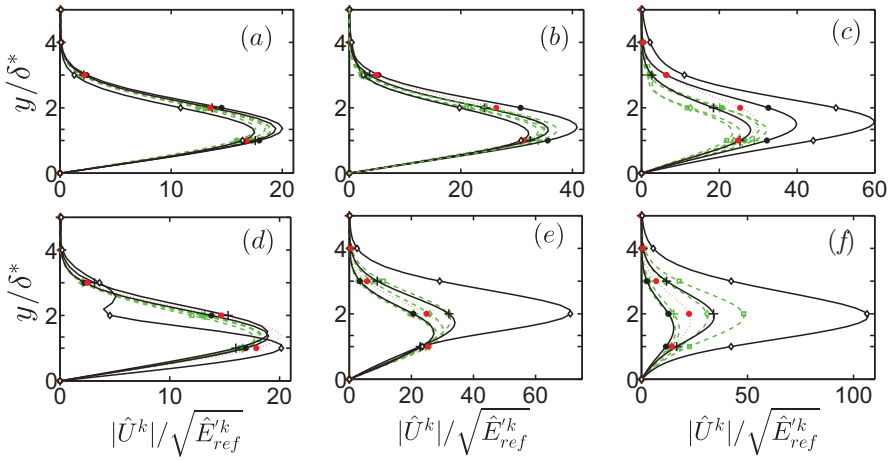

FIGURE 23. Streamwise velocity mode shapes for $k = 10$ at: (a)$R = 500$; (b) 1000; (c) 1500; and $k = 15$ at: (d)$R = 500$; (e) 1000; (f) 1500. Lines and markers as for figure 16. (colour online)

figure 22. The streamwise peak of energy is not observed in the streamwise domain for the $k = 10$ mode. The energy growth in the early layer is reduced relative to the Optimal streak which would show a linear line in the current scaling. Fransson *et al.* (2005*b*) noted a similar trend for FST induced Klebanoff streaks. The growth rates for the differing zither streaks also begins to differ downstream as the streak grows to amplitudes where non-linear effects are substantial. Presumably, non-linear effects cause the $\beta = 50\%$ with $\sigma_\delta = 0.075$ zither $k = 10$ mode to have the lowest scaled energy growth downstream.

All zither streaks except the $\beta = 50\%$ with $\sigma_\delta = 0.075$ zither show a streamwise energy peak for $k = 15$ that varies between $\overline{X} = 1$ and 1.6, i.e. downstream of the Optimal streak. The growth of the $\beta = 50\%$ with $\sigma_\delta = 0.075$ zither $k = 15$ mode grows rapidly beyond $\overline{X} = 1$ which indicates non-linear effects. Similar trends are found for the $k = 20$ and $k = 25$ modes.

The wall-normal modes shapes of $\hat{U}^k$ are shown in figure 23. For $k = 10$ (and $k = 5$ not shown), the maximum of the mode is at $y = 1.34\delta^*$, he same as the "universal" Klebanoff streak, or slightly above at larger streamwise distances. For $k = 15$ (and higher modes not shown), the maximum shifts away from the wall with increasing streamwise distance, creating wall-normal inflection points. Andersson *et al.* (2001) observed similar mode shapes for the non-linear streak generated by the Optimal disturbance.

5. Zither streak linear stability

The analysis suggests the zither streaks share many similarities with Klebanoff streaks, but are steady. If transition is to be predicted accurately in differing wind tunnels, then the methodology must be able to predict transition for the current zither streak base-flows. Watmuff (1998) observed that initial flow quality improvements related to the settling chamber screens shifted the transition location upstream to a distance 67% of that observed before the improvements. The computational results of Cossu & Brandt (2004) for the Optimal streak would suggest that transition was promoted in the Watmuff (1998) wind tunnel as TS growth was previously damped by the presence of streaks. However, Vaughan & Zaki (2011) found steady, free-stream forced streaks can increase TS growth rates. These studies did not use streaks generated from a realistic free-stream disturbance. Parabolized Stability Equations in three-dimensions (PSE-3D) will be used to assess the linear stability of the zither streak base-flows.

Conceptually, the PSE-3D can be used with the e^N method in place of the Orr-Sommerfeld or two-dimensional PSE equations. This would require a database of streaky base-flow transition results and would inherit all the limitations and assumptions of the e^N method, with no guarantee it will be as successful. The streaks affect on TS secondary instability, and streak secondary instability, are issues that should be considered. Here, only linear TS growth on the zither streak base-flow will be considered.

5.1. *PSE-3D and initial condition*

The growth of a small disturbance $q\left(x,y,z,t\right)=\left[u,v,w,p\right]^T$ on a steady, two-dimensional laminar base-flow can be described by the linear Parabolized Stability Equations (Bertolotti 1991). These equations can be extended to a three-dimensional base-flow (Broadhurst & Sherwin 2008; Paredes *et al.* 2011). Assuming the base-flow is spanwise periodic allows decomposition into spanwise Fourier modes by (4.10). The disturbance is formulated as the product of a shape function ($\hat{q}$) and wave-component,

$$q=\sum_{k=-\infty}^{\infty}\hat{q}\left(X,y\right)\exp\left(i\int_{x0}^{x}\alpha\left(\zeta\right).d\zeta+ik\beta z-i\omega t\right)+c.c, \tag{5.1}$$

where the shape function is assumed to vary on a slower streamwise scale, X, such that,

$$\frac{\partial}{\partial x}=\frac{\partial}{\partial X}\frac{\partial X}{\partial x}\equiv\frac{1}{Re}\frac{\partial}{\partial X}. \tag{5.2}$$

The streamwise wavenumber α is complex valued and ω, the disturbance circular frequency is real valued. The complex conjugate ($c.c$) creates a real-valued disturbance. The Floquet parameter is not included as the periodicity of the zither streak base-flows is multiple streaks wide and the physical relevance of a sub-harmonic or detuned disturbance is unclear. Even/odd assumptions are not made. The base-flow and α are assumed $O(1)$. Substituting (4.10) and (5.1) into the Linear Navier-Stokes equations and keeping terms $O\left(Re^{-1}\right)$ or greater leaves the three-dimensional, Parabolized Stability Equations (PSE-3D) formulated for a Cartesian geometry;

for a given k,

$$\sum_{j=-\infty}^{+\infty}A^{k-j}\hat{q}^j+B^{k-j}\hat{q}_y^j+C^{k-j}\hat{q}_{yy}^j+D^{k-j}\hat{q}_x^j=0, \tag{5.3}$$

where the matrices A, B, C, D are defined by,

$$\Delta = -i\omega^k\delta_{k,j} + i\alpha\hat{U}^{k-j} + ij\beta\hat{W}^{k-j} + \frac{\alpha^2+k^2\beta^2}{Re}\delta_{k,j}, \quad \delta_{k,j} = \begin{cases} 1 & k=j \\ 0 & k\neq j \end{cases}$$

$$A^{k-j} = \begin{bmatrix} \Delta+\hat{U}_x^{k-j} & \hat{U}_y^{k-j} & i\,(k-j)\,\beta\hat{U}^{k-j} & i\alpha\delta_{k,j} \\ \hat{V}_x^{k-j} & \Delta+\hat{V}_y^{k-j} & i\,(k-j)\,\beta\hat{V}^{k-j} & 0 \\ \hat{W}_x^{k-j} & \hat{W}_y^{k-j} & \Delta+i\,(k-j)\,\beta\hat{W}^{k-j} & ik\beta\delta_{k,j} \\ i\alpha\delta_{k,j} & 0 & ik\beta\delta_{k,j} & 0 \end{bmatrix},$$

$$B^{k-j} = \begin{bmatrix} \hat{V}^{k-j} & 0 & 0 & 0 \\ 0 & \hat{V}^{k-j} & 0 & \delta_{k,j} \\ 0 & 0 & \hat{V}^{k-j} & 0 \\ 0 & \delta_{k,j} & 0 & 0 \end{bmatrix},$$

$$C^{k-j} = \begin{bmatrix} -\frac{\delta_{k,j}}{Re} & 0 & 0 & 0 \\ 0 & -\frac{\delta_{k,j}}{Re} & 0 & 0 \\ 0 & 0 & -\frac{\delta_{k,j}}{Re} & 0 \\ 0 & 0 & 0 & 0 \end{bmatrix}, \; D^{k-j} = \begin{bmatrix} \hat{U}^{k-j} & 0 & 0 & \delta_{k,j} \\ 0 & \hat{U}^{k-j} & 0 & 0 \\ 0 & 0 & \hat{U}^{k-j} & 0 \\ \delta_{k,j} & 0 & 0 & 0 \end{bmatrix}.$$

Note, the effect of the $O\left(Re^{-1}\right)$ term α_x is assumed to be small and neglected. The majority of disturbance growth is forced in the wave-component by ensuring no energy growth of the shape function (Herbert 1997),

$$\int_0^L \int_0^{y_{max}} \left(\hat{u}^\dagger \cdot \hat{u}_x + \hat{v}^\dagger \cdot \hat{v}_x + \hat{w}^\dagger \cdot \hat{w}_x\right) dy.dz = 0. \tag{5.4}$$

The PSE-3D are solved by limiting the number of spanwise Fourier modes to some finite value. In the limit of a single Fourier mode, the two-dimensional PSE are recovered. The wall-normal (y) direction is differenced with Chebyshev polynomials via collocation on the Chebyshev–Gauss–Lobatto collocation points ($\overline{y}$) defined by,

$$\overline{y} = \cos\left(\frac{n\pi}{N_p}\right), \tag{5.5}$$

where p takes integer values from 0 to N_p, the number of collocation points used. The collocation points are mapped algebraically to the physical domain $[0 \ldots y_{max}]$ with,

$$y = a\frac{1+\overline{y}}{b-\overline{y}}, \; a = \frac{y_c y_{max}}{y_{max}-2y_c}, \; b = 1+\frac{2a}{y_{max}}, \tag{5.6}$$

where y_{max} is far-field position and half the collocation points are located below y_c. The shape function is differenced in the streamwise direction with an implicit backward Euler scheme. The PSE equations are ill-posed (Li & Malik 1997). To avoid numerical instability, a streamwise step size $\Delta x > \alpha_r^{-1}$ is used (Andersson *et al.* 1998; Broadhurst & Sherwin 2008). Further details of the implementation and verification cases can be found in Pook (2013).

An initial condition for the disturbance can be found from a BiGlobal stability analysis on a cross-stream (y, z) plane. The spatial, BiGlobal, polynomial eigenvalue problem can be derived from (5.3) as;

for a given k,

$$\sum_{j=-\infty}^{+\infty} L_1^{k-j}\hat{q}^j + L_2^{k-j}\hat{q}_y^j + C^{k-j}\hat{q}_{yy}^j = -\alpha D^{k-j}\hat{q}^j + \alpha^2 C^{k-j}\hat{q}^j, \tag{5.7}$$

where the matrices L_1, L_2, L_3, R_1, R_2 are defined by,

$$\Delta_2 = -i\omega^k\delta_{k,j} + ij\beta\hat{W}^{k-j} + \frac{k^2\beta^2}{Re}\delta_{k,j},$$

$$L_1^{k-j} = \begin{bmatrix} \Delta_2 & \hat{U}_y^{k-j} & i\,(k-j)\,\beta\hat{U}^{k-j} & 0 \\ 0 & \Delta_2 & 0 & 0 \\ 0 & \hat{W}_y^{k-j} & \Delta_2 + i\,(k-j)\,\beta\hat{W}^{k-j} & ik\beta\delta_{k,j} \\ 0 & 0 & ik\beta\delta_{k,j} & 0 \end{bmatrix},\ L_2^{k-j} = \begin{bmatrix} 0 & 0 & 0 & 0 \\ 0 & 0 & 0 & \delta_{k,j} \\ 0 & 0 & 0 & 0 \\ 0 & \delta_{k,j} & 0 & 0 \end{bmatrix},$$

Making the substitutions,

$$\hat{q} = \tilde{q}e^{-\alpha y}, \quad \hat{q}_y = \tilde{q}_y e^{-\alpha y} - \alpha\tilde{q}e^{-\alpha y}, \quad \hat{q}_{yy} = \tilde{q}_{yy}e^{-\alpha y} - 2\alpha\tilde{q}_y e^{-\alpha y} + \alpha^2\frac{\tilde{q}}{h_1^2}e^{-\alpha y}, \tag{5.8}$$

as used by Haj-Hariri (1988) with the Orr-Sommerfeld eigenvalue problem, reduces the polynomial eigenvalue problem to the general eigenvalue problem;

for a given k,

$$\sum_{j=-\infty}^{+\infty} L_1^{k-j}\tilde{q}^j + L_2^{k-j}\tilde{q}_y^j + C^{k-j}\tilde{q}_{yy}^j = -\alpha\left[\left(D^{k-j} - L_2^{k-j}\right)\tilde{q}^j - 2C^{k-j}\tilde{q}_y^j\right]. \tag{5.9}$$

The spatial eigenvalue problem (5.9) is solved with the same wall-normal differencing as the PSE-3D. In the limit of a single Fourier mode, the local stability problem (Orr-Sommerfeld equivalent) is retrieved.

For both the PSE-3D and BiGlobal problem, the disturbance is set to zero at the wall and far-field,

$$y\,(0) : u, v, w = 0, \quad y\,(y_{max}) : u, v, w = 0. \tag{5.10}$$

For all stability computations, 70 collocation points are used. Tests conducted by Pook (2013) indicate this is sufficient resolution for the accuracy desired.

5.2. *Two-dimensional base-flow linear stability*

The linear stability of the two-dimensional base-flow is shown by N-factor curves in figure 24. The N-factor measures the amplitude ratio growth of a disturbance from Branch 1, the streamwise position when the disturbance first becomes unstable, and is defined by,

$$N\text{-factor} = \int_{\text{Branch1}}^{x} \alpha_i . d\zeta \tag{5.11}$$

The CFD base-flow is of sufficient accuracy to provide results of at least qualitative accuracy (see Pook 2013) with approximately 40 CV through the layer in the wall-normal direction. A resolution check will be performed later with a zither streak base-flow.

5.3. *BiGlobal resolution of the eigenvalue spectrum*

The $\beta = 50\%$ with $\sigma_\delta = 0.075$ zither streak base-flow at $R = 940$ ($Re_{\delta^*} = 1615$) is used to examine spanwise resolution requirements. The streak peak amplitude (A) is 12.5%

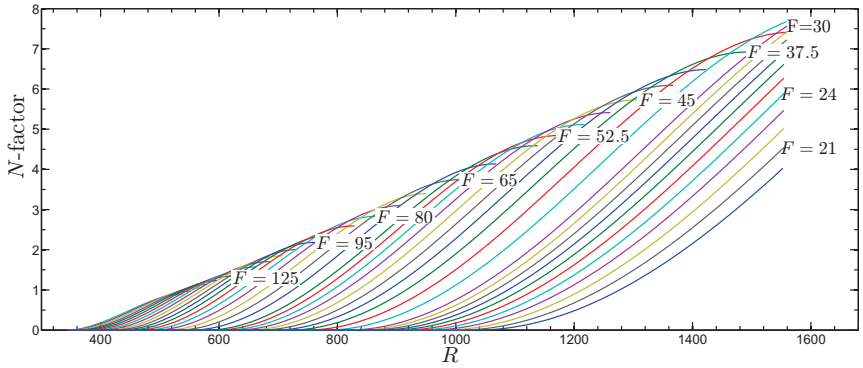

FIGURE 24. Two-dimensional base-flow N-factor curves calculated using PSE 5.3 with energy normalisation 5.4. (colour online)

and the standard deviation of amplitude (σ_A) is 5.4%. The BiGlobal eigenvalue spectrum is investigated for a disturbance non-dimensional frequency, $F = 65$ where,

$$F = \frac{\omega\nu}{U^2} \times 10^6. \tag{5.12}$$

The dimensional circular frequency is 326.8 rads^{-1}. For this frequency and position, the two-dimensional base-flow is unstable (slightly upstream of Branch 2).

The BiGlobal spectrum, calculated using the modes $k = -5$ to 5, is shown in figure (25) ($\alpha_i < 0$ indicates streamwise growth). The streaky base-flow is not symmetric which prevents using the even/odd assumption to reduce the eigenvalue problem size. The QZ eigenvalue solver (Matlab eig() function) is used. The spectrum is similar in appearance to that of two-dimensional Blasius flow. The discrete approximation to the continuous modes can be seen to the left of the spectrum. The spread of the continuous modes is due to the wall-normal differencing not capturing the oscillations of the eigenmodes. Four unstable, discrete eigenvalues can be seen near $\alpha\delta^* \approxeq 0.3$.

The eigenvalue spectrum in the region of the unstable eigenvalues is resolved more accurately using an increasing number of spanwise modes and the Arnoldi eigenvalue solver (Matlab eigs() function). The increased resolution produces a "curved line" of discrete eigenvalues. Similar to the spectrum for TS modes with varying spanwise wavenumber on a two-dimensional base-flow. The most unstable eigenvalue appears by itself. In the limit of two-dimensional flow, without providing direct proof, this mode would correspond to the two-dimensional TS mode. Tracking this mode back towards the leading edge (streak strength decreasing) produces an eigenmode with minimal spanwise variation and an eigenvalue close to that for the two-dimensional layer. It will be labelled the streaky TS mode following Cossu & Brandt (2004). The remaining eigenvalues can be seen to appear in pairs. In the limit of two-dimensional flow they would be the oblique TS modes. Each pair would converge to the same value as the flow becomes two-dimensional and the eigenmodes differ only in the spanwise propagation direction. They are split because the streaky zither base-flow is not spanwise symmetric. They will be labelled the streaky oblique TS modes.

With increasing resolution, the change in the computed eigenvalues reduces (see figure 25). A greater resolution is required to resolve the streaky oblique modes than the streaky TS mode. The convergence of the streaky TS mode eigenvalue (labelled A in figure 25) and shown in table does not change significantly beyond $k = 20$ modes. The

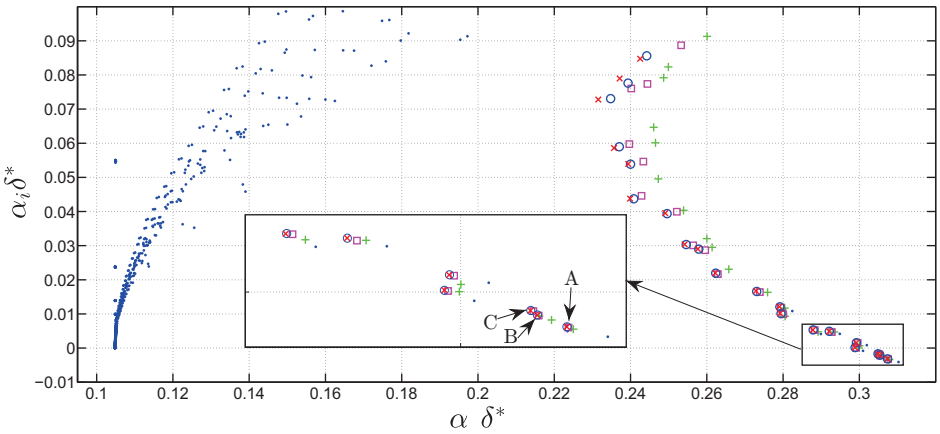

FIGURE 25. The effect of spanwise resolution (Fourier modes $k = -N$ to N) on the eigenvalues for the $\beta = 50\%$, $\sigma_\delta = 0.075$ zither at $Re_{\delta^*} = 1615$ ($R = 940$). Perturbation frequency is $F = 65$, $\omega = 326.8$ rad/s. A is streak TS mode. B and C are first streaky oblique TS modes. Markers: • $N = 5$ and QZ solver; + $N = 10$ and Arnoldi Solver; □ $N = 15$ and Arnoldi Solver; ○ $N = 20$ and Arnoldi Solver; × $N = 25$ and Arnoldi Solver. (colour online)

k	5	10	15	20	25
$\alpha_r\delta^*$	0.3103	0.3079	0.3075	0.3074	0.3074
$\alpha_i\delta^*$	$-0.004075i$	$-0.003384i$	$-0.003237i$	$-0.003167i$	$-0.003171i$

TABLE 3. Streaky TS mode convergence with BiGlobal spanwise resolution

majority of the streak base-flow energy is in wave-numbers below $k = 15$, and the streak spacing is approximately $k = 12$.

The eigenmodes of the streaky oblique TS modes (labelled B and C) are shown in figure 26. A spanwise resolution of $k = -25$ to 25 is used. The regions of increased u_{rms} are seen to be offset in the spanwise direction from each other. As for the streaky TS mode, the maxima of u_{rms} are located in the high-speed streak regions. The linear summation of the oblique modes is also shown in figure 26. The eigenmodes have been scaled to have the same total energy prior to addition. The majority of elevated u_{rms} for the combined streaky oblique modes is located to the left of $z/d = 500$ while the streaky TS mode is most elevated in regions the right of $z/d = 500$. The maximum spanwise velocity component of the streaky oblique modes, $\sim 0.6u_{rms}$ is considerably higher than that for the streaky TS mode, $\sim 0.4u_{rms}$ (not shown).

5.4. *Zither streak N-factor*

The effect of the zither wake on streaky TS growth and predicted transition is evaluated with N-factor curves. The curves are computed using the PSE-3D (5.3). The initial condition is provided by streaky TS mode of the BiGlobal spatial stability problem (5.9). The spanwise direction uses $k = -25$ to 25 Fourier modes.

Disturbance frequencies $F = 30$, 45, 65 are computed and the results are shown in figure 27. The $F = 30$ disturbance is also calculated using a base-flow mesh refined in each spatial direction by a factor of 1.5 in the boundary layer region (total mesh size ~ 125 million CV, ~ 60CV across the boundary layer). The mesh refinement modifies the calculated N-factor at $R = 1550$ by approximately 1%, an inconsequential error for

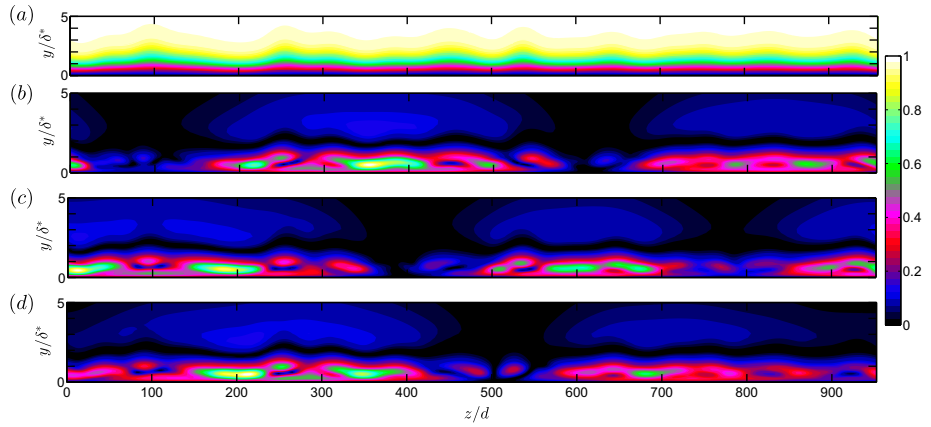

FIGURE 26. (*a*) Contours of the base-flow $\beta = 50\%$, $\sigma_\delta = 0.075$ zither at $Re_{\delta^*} = 1615$ ($R = 940$) streamwise velocity. (*b*) Streaky oblique TS mode , labelled B in figure 25, u_{rms} using Fourier modes $k = -25$ to 25. (*c*) Streaky oblique TS mode, labelled C in figure 25, u_{rms} using Fourier modes $k = -25$ to 25. (*d*) Addition of modes B and C, u_{rms}. (colour online)

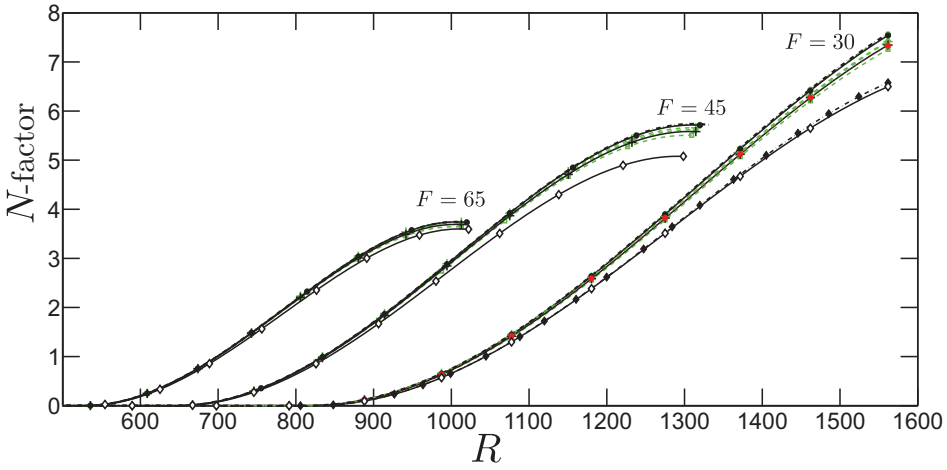

FIGURE 27. N-factor curves for the zither streak base-flows. Lines: —— Two-dimensional base-flow; -·-◆-·- $F = 30$ disturbance for $\beta = 50\%$ with $\sigma_\delta = 0.025$ zither CFD base-flow with increased mesh resolution; Other lines and markers as for figure 16. (colour online)

the current level of analysis. Increasing the resolution of the PSE-3D to 95 collocation points and $k = -32 \ldots 32$ modifies the N-factor by 0.5%.

The $F = 65$ disturbance reaches Branch 2, the streamwise position the disturbance becomes stable again, just downstream of $R = 1000$. The greatest suppression of the streaky TS is observed for the $\beta = 50\%$ with $\sigma_\delta = 0.075$ zither. However, the decrease in the Branch 2 N-factor is only 0.1.

The $F = 45$ TS mode reaches Branch 2 just downstream of $R = 1300$ on the two-dimensional base-flow. At $R = 1300$, the standard deviation of streak strength (σ_A) for the $\beta = 50\%$ with $\sigma_\delta = 0.075$ zither has reached 7.8%. The greater streamwise extent of TS and streak growth leads to greater suppression. For the $\beta = 50\%$ with $\sigma_\delta = 0.075$ zither, the reduction in the Branch 2 N-factor is 0.65. If transition were to occur due to this frequency, N-factor = 5 for the two-dimensional base-flow, then the predicted position to reach the same mode amplitude ratio would be delayed from $R = 1170$ to

$R = 1250$. For a wind tunnel velocity of 8.6 ms^{-1} and air, this corresponds to a shift from $x = 2.33$ m to $x = 2.66$ m; a delay of 15%. For the weaker zither streaks, the delay would be less than 3.5%.

The $F = 30$ disturbance Branch 2 N-factor is not observed in the streamwise domain. However, the suppression of TS growth is considerable. At $R = 1550$, the maximum reduction in N-factor is 1. If transition were to occur due to this frequency for the two-dimensional base-flow, N-factor = 6.5 $R = 1470$, then the $\beta = 50\%$ with $\sigma_\delta = 0.075$ zither would reach the same amplitude ratio at $R = 1560$. For the stated tunnel conditions, this corresponds to $x = 3.68$ m and $x = 4.15$ m. A delay of nearly 500 mm, or 12.6%. For all other zither wakes, the predicted delay is less than 100 mm, a delay of 2.7%.

The significant shift in the predicted transition location due to a zither more than 2 m upstream, with a standard deviation in wire position of only 38.1μm (15% of d), is supported by previously unexplained experimental observations. Watmuff (1998) replaced screens in his wind tunnel and observed a three-fold reduction in u_{rms} in the layer, indicating significantly weaker streaks. For this intermediate configuration (further flow quality improvements were made), turbulent bursting was observed to shift from $R \approx 1500$ upstream to $R \approx 1220$. For the two-dimensional layer, this corresponds to a reduction in N-factor from 7.3 ($F = 30$) to 5.4 ($F = 45$). Assuming the original tunnel configuration had streaks similar to the $\beta = 50\%$ with $\sigma_\delta = 0.075$ zither, then the original N-factor would have been 6. Assuming no streaks after installing the new screens and no change in TS initial amplitude, an N-factor of 6 would predict transition at approximately $R = 1300$ due to $F = 42.5$. This analysis over predicts the extent of laminar flow observed by 360 mm (13.5%), i.e. streaks present in the experiment may have provided even greater transition delay. A further possible contributory explanation is the streak influence on TS secondary instability, either delaying or promoting transition depending on the streak spanwise wavelength relative to the TS streamwise length (Liu *et al.* 2008*a*,*b*).

5.5. *Streaky TS eigenmode development*

The N-factor calculations use a single, global α for the entire cross-stream plane. This global value may not correlate well with transition, nor does it describe the distortion of the TS wave. Local α values along some defined path could be defined from the eigenmode and global α. However, local growth rates are not likely to be useful for the current streak base-flows.

Figures 28, 29 and 30 document the streaky TS eigenmode for the $\beta = 50\%$ with $\sigma_\delta = 0.075$ zither base-flow. The u_{rms} is significantly distorted from that of two-dimensional TS. At lower R with lower streak strength, the u_{rms} is seen to cluster into regions of high and low values with the maxima and minima located at approximately the same wall height. With increasing R, the peak in the low-speed streak regions move away from the wall, creating a spanwise zigzag pattern. Below this maximum, a visible minimum appears as a "hole" in the eigenvector. A wall-normal profile through this region shows an "M" shape. For the current results, the "M" generally has larger magnitude higher in the layer. This trend is similar to the observations of Fransson *et al.* (2005*a*) except they observed the higher layer peak to decrease with R until a similar value as the lower peak prior to Branch 2. It is interesting to note the visual wavelength differences for the disturbances at a similar streamwise position, $R = 900$ and 1000. The $F = 65$ disturbance near Branch 2, appears smoother with a larger dominant wavelength than the $F = 45$ and $F = 30$ disturbances.

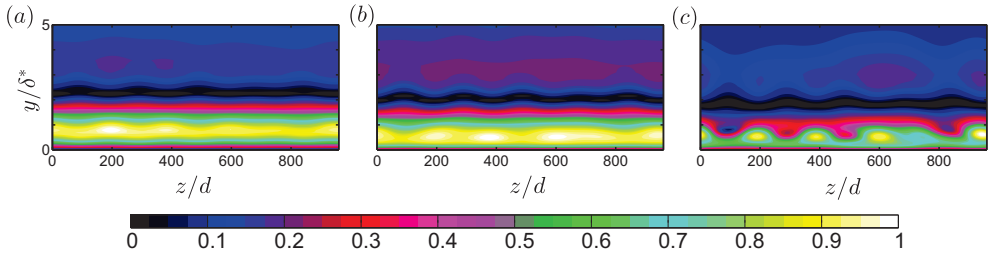

FIGURE 28. Streaky TS eigenmode u_{rms} for the $\beta = 50\%$ with $\sigma_\delta = 0.075$ zither, $F = 65$ at: (*a*) $R = 500$; (*b*) $R = 750$; (*c*) $R = 1000$. See insert for contour levels. (colour online)

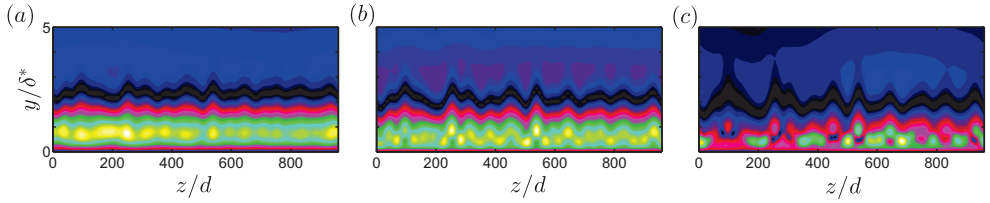

FIGURE 29. Streaky TS eigenmode u_{rms} for the $\beta = 50\%$ with $\sigma_\delta = 0.075$ zither, $F = 45$ at: (*a*) $R = 600$; (*b*) $R = 900$; (*c*) $R = 1200$. See figure 28 for contour levels. (colour online)

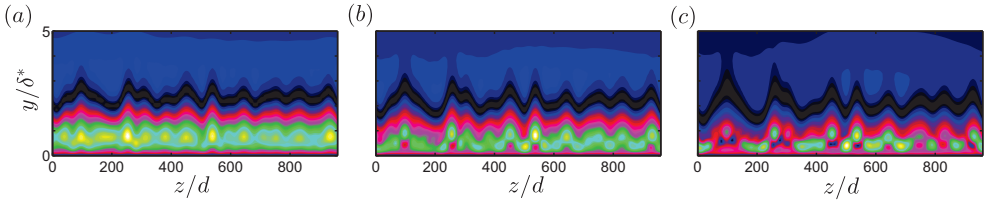

FIGURE 30. Streaky TS eigenmode u_{rms} for the $\beta = 50\%$ with $\sigma_\delta = 0.075$ zither, $F = 30$ at: (*a*) $R = 900$; (*b*) $R = 1200$; (*c*) $R = 1500$. See figure 28 for contour levels. (colour online)

5.6. *Streak secondary instability*

An extensive search for a streak secondary instability of the the $\beta = 50\%$ with $\sigma_\delta = 0.075$ zither streak base-flow at $R = 1550$ was conducted. The QZ method was used with up to 25 Fourier modes, and the Arnoldi method was used with up to 45 Fourier modes, searching the phase velocity region of 0.6 to 0.85. Streak secondary instability is known to occur at these phase velocities (Andersson *et al.* 2001). No secondary instability was detected. The streaky base-flow is still quite weak and only the results of Vaughan & Zaki (2011) would suggest a streak secondary instability may be present.

6. Discussion and conclusion

The linear diffusion equation with an initial condition from known wire position and drag produces good predictions of the far, steady, laminar wake. For the majority of zithers with a uniform inflow, the wake strength equation of Böttcher & Wedemeyer (1989) due to variation in wire position qualitatively captures the wake decay $\left(\overline{x}^{-0.75}\right)$ but under-predicts the wake strength. It was hypothesised that errors in wire position would modify wire drag and change the wake decay rate from $\overline{x}^{-0.75}$ towards $\overline{x}^{-0.25}$, producing stronger far wakes. The majority of CFD results did not support this hypothesis. The drag variation induced failed to excite large wavelengths. However, the $\beta = 50\%$ with $\sigma_\delta = 0.075$ zither did induce substantial large wavelength drag variation relative

to shorter wavelengths and the far wake decay was seen to alter. Flow visualisation at the zither showed isolated instance of jet deflection, but not as significant as previous experimental visualisations (comparing contours plots from computations to experimental flow visualisation may be a contributory factor). In the context of the linear diffusion equation, explaining a significantly stronger far wake in terms of the coalescence of jets is problematic. This phenomena occurs over a short wavelength, i.e. the pairing, tripling, etc., of jets is wavelengths of the order of $2M$. Short wavelengths have no influence on the far wake. Supporting the proposition that the coalescence of jets is not responsible for increased spanwise variation of the test-section layer is the drag data of the $\beta = 40\%$ with $\sigma_\delta = 0.025$ zither. This zither exhibited a unique Fourier spectrum for drag with relatively large increases at high wavenumbers approaching that for a wavelength $2M$. Flow visualisation revealed more significant instances of jet deflection relative to the $\beta = 50\%$ with $\sigma_\delta = 0.075$ zither yet the spanwise variation in the test-section layer was reduced.

Based on the zither simulations, it can be hypothesised that for a given open-area ratio, there is an allowable variation in wire position (σ_δ) above which large wavelengths of drag are excited and the far wake will become stronger, e.g. $\sigma_\delta = 0.075$ for $\beta = 50\%$. Instances of jet deflection may be apparent (a symptom) but it is not a cause. The allowable variation in wire position is likely to be Reynolds number dependant. Lower Reynolds numbers reduce the change in drag (pressure drop) of a perfect zither relative to open-area ratio, thus larger errors in wire position will be required to induce significant variations at lower Reynolds numbers. This may also explain the less substantial jet deflection in the current simulations relative to previous flow visualisations. Another consideration is the steady simulations may prevent a flow instability developing that creates a different jet pattern. This would require time-dependant simulations to assess.

Screens may produce wakes in better agreement with the combined wake equation (far wake $\propto \overline{x}^{-0.25}$) as there is a variation in drag across the screen where wires intersect. Assuming each intersection has a slightly different drag, then it would be expected that large wavelengths that most zithers failed to excite, would be present. Support for this proposition can be found in the experimental measurements of screen wake strength by Böttcher & Wedemeyer (1989). For two of the three screens tested, the wake decay substantially deviated from $\overline{x}^{-0.75}$ towards $\overline{x}^{-0.25}$ beyond $\overline{x} \simeq 1$. Interestingly, the lowest open-area ratio screen tested ($\beta = 53\%$) did not exhibit the wake decay change in the observed streamwise domain. The zither simulations would suggest a non-uniform inflow could produce the observed response. However, the experiments towed the screens through a water tank, eliminating non-uniform inflow as a factor.

The zither wakes from a non-uniform inflow showed increasingly stronger far wakes, relative to a uniform inflow, with increasing open-area ratio. The non-uniform inflow with large wavelength velocity variation induced large wavelength drag variations and hence, wake decay tending to $\overline{x}^{-0.25}$. However, with decreasing open-area ratio, the drag variation induced becomes near equal and opposite to the contribution of the non-uniform inflow, cancelling out the non-uniform inflow as predicted by Taylor & Batchelor (1949). The wake of the $\beta = 40\%$ with $\sigma_\delta = 0.025$ zither was near invariant to the non-uniform inflow. This result indicates that low open-area ratio screens should be used to remove flow non-uniformity. However, a physically constructed screen (zither) will have some dimensional error (ϵ) introduced by the manufacturing process (say σ_ϵ). This will create a wake described the equation of Böttcher & Wedemeyer (1989). From (2.27), the wake strength is found to be dependant on the product,

$$\overline{q}\,(Re, \beta)\,\frac{\sigma_\epsilon}{\sqrt{M}}. \tag{6.1}$$

The mean source strength increases rapidly (non-linearly) with decreasing open-area ratio (see figure 5.1 of Pook 2013) while M decreases linearly (for a zither) and σ_ϵ is a constant. Hence, the imperfect, low-open area ratio zither can have a significantly stronger far wake despite cancelling the non-uniform inflow. The onset of increased wake strength could appear rapidly with a small change in open-area ratio. The non-dimensional standard deviation of position error σ_δ will increase and this could further increase the far wake strength if large wavelength drag variation is induced, as was observed for the $\beta = 50\%$ with $\sigma_\delta = 0.075$ zither with a uniform inflow. Increased far wake strengths can be ascribed without resorting to the coalescence of jet phenomena.

Explaining increased spanwise variation of the test-section layer also requires understanding the path of the wake in a given wind tunnel. Contractions are widely used in wind tunnels, allowing screens to be placed in slower flow which reduces pressure losses and increases efficiency. They also reduce the variation of the test-section, streamwise velocity variation in proportion to the the inverse of the contraction ratio, and reduce free-stream u_{rms}turbulence levels. What is perhaps less well appreciated, is normal vorticity entering the contraction will be tilted and stretched into streamwise vorticity. The stretching of a 5:1 contraction can cancel out a significant amount of wake decay near the contraction boundaries by converting it to streamwise vorticity. At the measurement location downstream of the contraction, the streamwise vorticity exiting was 30% to 45% of the normal vorticity entering. The wake exiting the contraction will be nearly immeasurable in terms of streamwise velocity (largest variation 0.015% of U) or pressure, but streamwise vorticity is present. Boundary layers are most receptive to low frequency, streamwise vorticity (Schrader *et al.* 2010) and this vortical disturbance can undergo considerable non-modal/algebraic growth in the boundary layer (Andersson *et al.* 1999; Levin & Henningson 2003; Luchini 2000). The unsuspecting experimentalist can be left with significant spanwise variation of the test-section boundary layer, no measure of the free-stream to correlate with, and no understanding of how the disturbance originated. Designing a wind tunnel to minimise the variation of the streamwise velocity in the test-section may lead to increased spanwise variation of the test-section layer, particularly if poor quality screens are used.

The Böttcher & Wedemeyer (1989) theory provides an explanation for consistent Klebanoff streak spacing between differing experiments, that is not necessarily seen in computations that use 'artifical' free-stream turbulence. The wake wavelength is predicted to be independent of zither geometry. This agrees with Matsubara & Alfredsson (2001) who observed physically constant Klebanoff streak spacing with differing disturbance grids. It also concurs with the results of Swearingen & Blackwelder (1987) who found that the spacing of Görtler vortices was unaffected by changing the screen mesh size or the position of the final settling chamber screen, but the spacing pattern was dependent on the individual screen and repeatable. The apparent insensitivity to the screen streamwise location could be attributed to the $x^{0.5}$ dependence of the wake wavelength, combined with large x. The wavelength will not change significantly downstream of a moderate or high contraction ratio due to the reduced time for diffusion in the higher speed flow.

The spanwise variation of the test-section boundary layer generated by some of the uniform inflow zither wakes was substantial. The most substantial streaks were caused by the $\beta = 50\%$ with $\sigma_\delta = 0.075$ zither which had the strongest wake. The maximum streak amplitude (A) at $R = 1500$ was approximately 20%. The standard deviation of streak amplitude (σ_A) was 9%. The maximum variation in the layer displacement thickness ($\Delta\delta^*$) was 70%, and the skin friction variation ($\sigma_{cf}/\overline{cf}$) was 17%. The skin friction variation is of the order measured by Bradshaw (1965) in a turbulent layer and attributed to the coalescence of jets. It should be noted that the uniform inflow zither

streaks set a lower bound for spanwise variation in the wind tunnel configuration used. Non-uniform inflow, a reason for a using a screen, can be expected to increase spanwise variation for common screen open-area ratios ($\beta > 57\%$).

The streaks generated by the zither wakes exhibited similar characteristics to Klebanoff streaks. The free-stream disturbance, in terms of streamwise velocity, was near immeasurable (Watmuff 1998). Streak growth was reduced at low R (Fransson *et al.* 2005*b*) but nearly linear with $x^{0.5}$ till beyond $R > 1000$ (Westin *et al.* 1994). Wall-normal profiles of the Fourier modes in the streak exhibited a maximum at $y = 1.34\delta^*$ (Westin *et al.* 1994; Kendall 1985, 1998). However, with increasing R shorter wavelength modes (increasing k) would show a maximum shifting away from the wall and the mode energy would increase rapidly. Physical profiles showed that the low-speed region of the streak would lift away from the wall (Jacobs & Durbin 2001) while the high-speed region would move towards the wall (Nolan & Walsh 2012). The spanwise wavelength of the streaks was a near constant physical distance (Ovchinnikov *et al.* 2008) and dictated by the free-stream (Fransson & Alfredsson 2003). The streaks cause the spanwise mean shape factor to decrease with streamwise distance (Westin *et al.* 1994). The mean velocity profile deviation from the base-flow generally develops an "s" shape with increasing R, in agreement with Westin *et al.* (1994) but disagreement with Kendall (1985). The major characteristic not captured is the possible unsteadiness of Klebanoff streaks.

Directly relating streak amplitude to a zither, or the zither wake strength upstream of the contraction, was not achieved. The ratio of the standard deviation of streak amplitude, to the standard deviation of the wake strength entering the contraction ($\sigma_A/\sigma_{\Delta u/U\,in}$), varied between 4.5 and 10.5 at $R = 1500$. Larger open-area ratio zithers and smaller wire position errors (σ_δ) collapsed closely to 4.5. With decreasing open-area ratio and increasing wire position error, this ratio increased. This is attributed to the zither creating stronger, large wavelength modes due to the increasing variation in drag across the zither. The ratio $\sigma_A/\sigma_{\Delta u/U\,in}$ will be wind tunnel dependent.

The $\beta = 50\%$ with $\sigma_\delta = 0.075$ zither is the only zither predicted to have a significant effect on the transition location. The effect was predicted using the PSE-3D equations and computing the reduction in N-factor using a global growth rate. For $F = 30$, the N-factor growth was reduced by 1 in the streamwise domain (Branch 2 was not reached). This is predicted to shift the the predicted transition location by more than 10%. The predicted shift in transition is solely attributable to random errors in the position of the wires constructing the zither. The standard deviation of the wire position errors is only 38.1μm (15% of the wire diameter) and the zither is located nearly 2.3m upstream. However, the validity of using a spanwise global growth rate to predict and correlate with transition is untested although a greater than 10% shift in transition due to streaks seems possible (see Watmuff 1998). The Tollmien-Schlichting mode shapes are significantly altered by the presence of the streaks, and this may have significant effects on TS secondary instability not considered in the current analysis (Liu *et al.* 2008*b*). Weaker streaks may also significantly affect experiments where the disturbance growing has a low frequency, streamwise vorticity dependence, e.g. Görtler instability (Swearingen & Blackwelder 1986).

All the zither streaks studied stabilised TS in the streamwise region examined. This is consistent with the behaviour of the Optimal streak (Cossu & Brandt 2004; Bagheri & Hanifi 2007; Schlatter *et al.* 2011), steady roughness or vortex generated streaks (Fransson *et al.* 2005*a*, 2006; Shahinfar *et al.* 2012), and Klebanoff streaks (Arnal & Juillen 1978; Boiko *et al.* 1994; Watmuff 1998). However, it contrasts the results of Vaughan & Zaki (2011) that generated streaks from the free-stream with a Squire mode and found they could destabilise TS. This suggests the source of the disturbance that generates

the streak is important when determining its affect on TS. Combined with the aforementioned experimental results, it indicates that Klebanoff streaks generated from a screen/grid/zither are stabilising. However, Kendall (1991) has experimentally observed increased TS wave-packet growth in the presence of Klebanoff streaks generated from a disturbance upstream of the contraction. More work is required to explain the anomalous observations.

A secondary streak instability was not detected for the zither streak base-flows. No secondary streak instability would be expected based on the amplitude thresholds for the Optimal streak (Andersson *et al.* 2001), but the thresholds of Vaughan & Zaki (2011) for a streak generated from the free-stream (steady Squire mode) would have predicted a streak secondary instability for the $\beta = 50\%$ with $\sigma_\delta = 0.075$ zither streaks.

The current simulations have focused on streaks generated from normal vorticity that is tilted and stretched into streamwise vorticity in a contraction upstream of the test-section leading edge. Streamwise vorticity will also be present upstream of the contraction when using a screen, and it will be stretched in a contraction. Stretching would be a maximum on the tunnel centreline. However, a small CFD simulation of a perfect, single screen element (four square wires bounding a hole, not shown) revealed the normal vorticity to decay less rapidly than the streamwise vorticity, leading to orders of magnitude greater normal vorticity downstream. This suggests, at least for steady laminar flow, that normal vorticity entering the contraction is most likely the cause of streamwise vorticity in the test-section. The current simulations would then be the worst case scenario; normal vorticity through a two-dimensional contraction on to a flat-plate near the wind tunnel floor. Conversely, the best case scenario for a wind tunnel using screens and not a zither would be a two-dimensional contraction with the plate located on the tunnel centreline (expect minimal streamwise vorticity on the centreline) although a three-dimensional contraction will produce less streamwise vorticity across the entire cross-section.

The current analysis of the steady zither wake is readily extended to another spatial dimension. The major issue would be modelling the drag/source variation of a screen. It might be simpler to consider the holes in the screen as point sources of "thrust". How this varies with non-uniformities in screen weave is an open question.

Understanding that spanwise variation can be attributed to weak streamwise vorticity offers the potential to allow for its affects on experimental results. Streamwise vorticity can be detected as the spatial variation of flow angle. The strongest zither wake produced a maximum flow angle of 0.26°, just upstream of the leading edge. The standard deviation of the flow angle at the leading edge was only 0.1°. Flow angle measurements could be used for streak prediction if sampled at a resolution adequate to resolve the streamwise vorticity. Böttcher & Wedemeyer (1989) theory and non-modal growth theory could be used to design a flow quality survey that will provide an accurate assessment of the streamwise vorticity present. This information, combined with receptivity data for streamwise vorticity, could be used to predict the streaks in a layer and then assess their affect on e^N transition calculations. Streak effects could then be removed from test data, possibly improving transition correlation between differing wind tunnels, and wind tunnels and the intended operating environment.

Ultimately, all disturbances in the wind tunnel need to be related to their source if accurate transition predictions are to be made. Engineers conducting transition studies in a wind tunnel must not think what is the transition mechanism and region for the given body, but what is the transition mechanism and region for the given body in the given wake/disturbance environment. The work presented links steady streaks in the test-section layer to their origin at imperfect zithers (wind tunnel settling screen model) and studied their predicted affect on transition. The original analysis of Böttcher &

Wedemeyer (1989) provides a relation between the wake that will generate streaks and an imperfect zither. Including the variation of drag has been shown to be important. With simple relations such as these, the wind tunnel designer may be able to better quantify screens and their wakes. Extending this work will hopefully lead to improved transition prediction and correlation between differing wind tunnels.

D.A. acknowledges funding from the Australian Postgraduate Award (APA). Access to the Trifid HPC cluster provided by the V3 Alliance and the assistance of the RMIT eResearch Office is gratefully acknowledged

REFERENCES

Andersson, P., Berggren, M. & Henningson, D. S. 1999 Optimal Disturbances And Bypass Transition In Boundary Layers. *Physics of Fluids* **11** (1), 134–150.

Andersson, P., Brandt, L., Bottaro, A. & Henningson, D. S. 2001 On The Breakdown Of Boundary Layer Streaks. *Journal of Fluid Mechanics* **428**, 29–60.

Andersson, P., Henningson, D. S. & Hanifi, A. 1998 On A Stabilization Procedure For The Parabolic Stability Equations. *Journal of Engineering Mathematics* **33** (3), 311–332.

Arnal, D. & Juillen, J. C. 1978 Contribution Experimentale a l'etude de la Receptivite d'un Couche Limite Laminaire, a la Turbulence de l'ecoulement General- ONERA Rt. Tech. no. 1/5018 AYD. *Tech. Rep.*. ONERA.

Asai, M., Minagawa, M. & Nishioka, M. 2002 The Instability And Breakdown Of A Near-Wall Low-Speed Streak. *Journal of Fluid Mechanics* **455**, 289–314.

Bagheri, S. & Hanifi, A. 2007 The Stabilizing Effect Of Streaks On Tollmien-Schlichting And Oblique Waves: A Parametric Study. *Physics of Fluids* **19**, 19–22.

Batchelor, G. K. 2000 *An Introduction to Fluid Dynamics*, 2nd edn. Cambridge University Press.

Bell, J. H. & Mehta, R. D. 1990 Development Of A Two-Stream Mixing Layer From Tripped And Untripped Boundary Layers. *AIAA Journal* **28** (12), 2034–2042.

Bertolotti, F. P. 1991 Linear And Nonlinear Stability Of Boundary Layers With Streamwise Varying Properties. PhD thesis, Ohio State University.

Bohl, J. G. Elder v. 1940 Das Verhalten Paralleler Luftstrahlen. *Ingenieur-Archiv* **11** (4), 295–314.

Boiko, A. V., Westin, K. J. A., Klingmann, B. G. B., Kozlov, V. V. & Alfredsson, P. H. 1994 Experiments In A Boundary Layer Subjected To Free Stream Turbulence. Part 2. The Role Of Ts-Waves In The Transition Process. *Journal of Fluid Mechanics* **281**, 219–245.

Böttcher, J. & Wedemeyer, E. 1989 The Flow Downstream Of Screens And Its Influence On The Flow In The Stagnation Region Of Cylindrical Bodies. *Journal of Fluid Mechanics* **204**, 501–522.

Bradshaw, P. 1965 The Effect Of Wind-Tunnel Screens On Nominally Two-Dimensional Boundary Layers. *Journal of Fluid Mechanics* **22** (4), 679–687.

Brandt, L. & Henningson, D. S. 2002 Transition Of Streamwise Streaks In Zero-Pressure-Gradient Boundary Layers. *Journal of Fluid Mechanics* **472**, 229–261.

de Bray, B. G. 1967 Some Investigations Into The Spanwise Non-Uniformity Of Nominally Two-Dimensional Incompressible Boundary Layers Downstream Of Gauze Screens- Reports And Memoranda No. 3578. *Tech. Rep.*. Aeronautical Research Council.

Broadhurst, M. S. & Sherwin, S. J. 2008 The Parabolised Stability Equations for 3D-Flows: Implementation and Numerical Stability. *Applied Numerical Mathematics* **58** (7), 1017–1029.

Butler, K. M. & Farrell, B. F. 1992 Three-Dimensional Optimal Perturbations In Viscous Shear Flow. *Physics of Fluids A: Fluid Dynamics* **4** (8), 1637–1650.

Cheng, M. & Moretti, P. M. 1988 Experimental Study Of The Flow Field Downstream Of A Single Tube Row. *Experimental Thermal and Fluid Science* **1** (1), 69–74.

Corrsin, S. 1944 Investigation Of The Behavior Of Parallel Two-Dimensional Air Jets: NASA-TM-101182. *Tech. Rep.*. NACA.

Cossu, C. & Brandt, L. 2004 On Tollmien-Schlichting-like waves in streaky boundary layers. *European Journal of Mechanics - B/Fluids* **23** (6), 815–833.

Crow, S. C. 1966 The Spanwise Perturbation Of Two-Dimensional Boundary Layers. *Journal of Fluid Mechanics* **24** (1), 153–164.

Dengel, P. & Fernholz, H. H 1989 Generation Of And Measurements In A Turbulent Boundary Layer With Zero Skin Friction. In *In Advances in Turbulence 2* (ed. H.H. Fernholz & H.E. Fiedler), pp. 432–437. Springer Berlin Heidelberg.

Ellingsen, T. & Palm, E. 1975 Stability Of Linear Flow. *Physics of Fluids* **18** (4), 487–488.

Ertunç, Ö., Özyilmaz, N., Lienhart, H., Durst, F. & Beronov, K. 2010 Homogeneity Of Turbulence Generated By Static-Grid Structures. *Journal of Fluid Mechanics* **654**, 473–500.

Fransson, J. H. M. & Alfredsson, P. H. 2003 On The Disturbance Growth In An Asymptotic Suction Boundary Layer. *Journal of Fluid Mechanics* **482**, 51–90.

Fransson, J. H. M., Brandt, L., Talamelli, A. & Cossu, C. 2004 Experimental And Theoretical Investigation Of The Nonmodal Growth Of Steady Streaks In A Flat Plate Boundary Layer. *Physics of Fluids* **16** (10), 3627–3638.

Fransson, J. H. M., Brandt, L., Talamelli, A. & Cossu, C. 2005*a* Experimental Study Of The Stabilization Of Tollmien-Schlichting Waves By Finite Amplitude Streaks. *Physics of Fluids* **17** (5), 054110.

Fransson, J. H. M., Matsubara, M. & Alfredsson, P. H. 2005*b* Transition Induced By Free-Stream Turbulence. *Journal of Fluid Mechanics* **527**, 1–25.

Fransson, J. H. M., Talamelli, A., Brandt, L. & Cossu, C. 2006 Delaying Transition To Turbulence By A Passive Mechanism. *Physical Review Letters* **96** (6), 064501.

Goldstein, M. E. & Leib, S. J. 1993 Three-Dimensional Boundary-Layer Instability And Separation Induced By Small-Amplitude Streamwise Vorticity In The Upstream Flow. *Journal of Fluid Mechanics* **246**, 21–41.

Goldstein, M. E., Leib, S. J. & Cowley, S. J. 1992 Distortion Of A Flat-Plate Boundary Layer By Free-Stream Vorticity Normal To The Plate. *Journal of Fluid Mechanics* **237**, 231–260.

Hack, M.J.P. & Zaki, T.A. 2014 Streak instabilities in boundary layers beneath free-stream turbulence. *Journal of Fluid Mechanics* **741**, 280–315.

Haj-Hariri, H. 1988 Transformations Reducing The Order Of The Parameter In Differential Eigenvalue Problems. *Journal of Computational Physics* **77** (2), 472–484.

Hancock, P. E. 1998 Plane Multiple Screens In Non-Uniform Flow, With Particular Application To Wind Tunnel Settling Chamber Screens. *European Journal of Mechanics - B/Fluids* **17** (3), 357–369.

Herbert, T. 1988 Secondary Instability Of Boundary Layers. *Annual Review of Fluid Mechanics* **20**, 487–526.

Herbert, T. 1997 Parabolized Stability Equations. *Annual Review of Fluid Mechanics* **29**, 245–283.

Hultgren, L. S. & Gustavsson, L. H. 1981 Algebraic Growth Of Disturbances In A Laminar Boundary Layer. *Physics of Fluids* **24** (6), 1000–1004.

Jacobs, R. G. & Durbin, P. A. 2001 Simulations Of Bypass Transition. *Journal of Fluid Mechanics* **428**, 185–212.

Kendall, J. M. 1985 Experimental Study of Disturbances Produced In A Pre-Transitional Laminar Boundary Layer by Weak Freestream Turbulence: AIAA-85-1695. In *18th Fluid Dynamics and Plasmadynamics and Lasers Conference, July 16-18*, pp. 1–10. Cincinatti, Ohio: AIAA.

Kendall, J. M. 1991 Studies On Laminar Boundary-Layer Receptivity To Freestream Turbulence Near A Leading Edge: FED-VOL. 114. In *Boundary Layer Stability and Transition to Turbulence*, pp. 23–30. Portland, Oregon: ASME.

Kendall, J. M. 1998 Experiments On Boundary-Layer Receptivity To Freestream Turbulence: AIAA-98-0530. In *36th Aerospace Sciences Meeting & Exhibit, Jan 12-15*, pp. 1–14. Reno, NV: AIAA.

Klebanoff, P. S. 1971 Effect Of Freestream Turbulence On A Laminar Boundary Layer. *Bulletin of The American Physical Society* **10**.

Klebanoff, P. S., Tidstrom, K. D. & Sargent, L. M. 1961 The Three-Dimensional Nature Of Boundary-Layer Instability. *Journal of Fluid Mechanics* **12**, 1–42.

Le Gal, P., Peschard, I., Chauve, M. P. & Takeda, Y. 1996 Collective Behavior Of Wakes Downstream A Row Of Cylinders. *Physics of Fluids* **8** (8), 2097–2106.

Leib, S. J., Wundrow, D. W. & Goldstein, M. E. 1999 Effect Of Free-Stream Turbulence And Other Vortical Disturbances On A Laminar Boundary Layer. *Journal of Fluid Mechanics* **380**, 169–203.

Levin, O. & Henningson, D. S. 2003 Exponential Vs Algebraic Growth And Transition Prediction In Boundary Layer Flow. *Flow, Turbulence and Combustion* **70**, 183–210.

Li, F. & Malik, M. R. 1997 Spectral Analysis Of Parabolized Stability Equations. *Computers & fluids* **26** (3), 279–297.

Liu, Y., Zaki, T. A. & Durbin, P. A. 2008*a* Boundary-Layer Transition By Interaction Of Discrete And Continuous Modes. *Journal of Fluid Mechanics* **604**, 199–233.

Liu, Y., Zaki, T. A. & Durbin, P. A. 2008*b* Floquet Analysis Of Secondary Instability Of Boundary Layers Distorted By Klebanoff Streaks And Tollmien-Schlichting Waves. *Physics of Fluids* **20** (12), 124102.

Loehrke, R. I. & Nagib, H. M. 1972 Experiments On Management Of Free-Stream Turbulence: AGARD-R-598. *Tech. Rep.* 598. AGARD.

Luchini, P. 2000 Reynolds-Number-Independent Instability Of The Boundary Layer Over A Flat Surface : Optimal Perturbations. *Journal of Fluid Mechanics* **404**, 289–309.

Matsubara, M. & Alfredsson, P. H. 2001 Disturbance Growth In Boundary Layers Subjected To Free-Stream Turbulence. *Journal of Fluid Mechanics* **430**, 149–168.

Mehta, R. D. 1985 Turbulent Boundary Layer Perturbed By A Screen. *AIAA journal* **23** (9), 1335–1342.

Mehta, R. D. & Bradshaw, P. 1979 Design Rules For Small Low Speed Wind Tunnels. *The Aeronautical Journal of the Royal Aeronautical Society* .

Mehta, R. D. & Hoffmann, P. H. 1987 Boundary Layer Two-Dimensionality In Wind Tunnels. *Experiments in Fluids* **5** (5), 358–360.

Morgan, P. G. 1960 The Stability Of Flow Through Porous Screens. *Journal of The Royal Aeronautical Society* **64** (June), 359–362.

Morkovin, M.V. 1979 On The Question Of Instabilities Upstream Of Cylindrical Bodies-NASA-CR3231. *Tech. Rep.* December.

Morkovin, M. V. 1969 On The Many Faces Of Transition. In *Viscous Drag Reduction* (ed. C.S. Wells). Plenum, New York.

Nolan, K. P. & Walsh, E. J. 2012 Particle Image Velocimetry Measurements Of A Transitional Boundary Layer Under Free Stream Turbulence. *Journal of Fluid Mechanics* **702**, 215–238.

Nugroho, B., Hutchins, N. & Monty, J. P. 2013 Large-Scale Spanwise Periodicity In A Turbulent Boundary Layer Induced By Highly Ordered And Directional Surface Roughness. *International Journal of Heat and Fluid Flow* **41**, 90–102.

Ovchinnikov, V., Choudhari, M. M. & Piomelli, U. 2008 Numerical Simulations Of Boundary-Layer Bypass Transition Due To High-Amplitude Free-Stream Turbulence. *Journal of Fluid Mechanics* **613**, 135–169.

Paredes, P., Theofilis, V., Rodríguez, D. & Tendero, J. A. 2011 The Pse-3D Instability Analysis Methodology For Flows Depending Strongly On Two And Weakly On The Third Spatial Dimension: AIAA-2011-3752. In *6th AIAA Theoretical Fluid Mechanics Conference 27-30 June 2011*. Honolulu, Hawaii: AIAA.

Patel, R. P. 1964 The Effects Of Wind Tunnel Screens And Honeycombs On The Spanwise Variation Of Skin Friction In Two-Dimensional Turbulent Boundary Layers- T/N 64-7. *Tech. Rep.* 7. McGill University.

Pook, D.A. 2013 The Origin and Effects of Free-Stream Vortical Disturbances on Boundary Layer Transition in Wind Tunnels. Phd, RMIT University.

Pook, D.A. & Watmuff, J.H. 2014 Streak generation in wind tunnels. *Physics of Fluids* **26** (7), 073605.

Reddy, S.C., Schmid, P.J. & Henningson, D.S. 2008 Pseudospectra of the Orr-Sommerfeld Operator. *Siam Journal on Applied Mathematics* **53** (1), 15–47.

Reynolds, R. T., Hayden, P., Castro, I. P. & Robins, A. G. 2006 Spanwise Variations In

Nominally Two-Dimensional Rough-Wall Boundary Layers. *Experiments in Fluids* **42** (2), 311–320.

Ricco, P. 2009 The Pre-Transitional Klebanoff Modes And Other Boundary-Layer Disturbances Induced By Small-Wavelength Free-Stream Vorticity. *Journal of Fluid Mechanics* **638**, 267.

Ricco, P., Luo, J. & Wu, X. 2011 Evolution And Instability Of Unsteady Nonlinear Streaks Generated By Free-Stream Vortical Disturbances. *Journal of Fluid Mechanics* **677**, 1–38.

Schlatter, P., Brandt, L., de Lange, H. C. & Henningson, D. S. 2008 On Streak Breakdown In Bypass Transition. *Physics of Fluids* **20** (10), 101505.

Schlatter, P., Deusebio, E., de Lange, R. & Brandt, L. 2011 Numerical Study Of The Stabilisation Of Boundary-Layer Disturbances By Finite Amplitude Streaks. *Tech. Rep.*. Swedish e-Science Research Centre, Linne FLOW Centre, KTH Mechanics, Stockholm, Sweden.

Schmid, P. J. 2007 Nonmodal Stability Theory. *Annual Review of Fluid Mechanics* **39**, 129–162.

Schrader, L., Brandt, L., Mavriplis, C. & Henningson, D. S. 2010 Receptivity To Free-Stream Vorticity Of Flow Past A Flat Plate With Elliptic Leading Edge. *Journal of Fluid Mechanics* **653**, 245–271.

Schubauer, G. B., Spangenberg, W. G. & Klebanoff, P. S. 1950 Aerodynamic Characteristics Of Damping Screens: TN 2001. *Tech. Rep.*. NACA.

Shahinfar, S., Sattarzadeh, S. S., Fransson, J. H. M. & Talamelli, A. 2012 Revival Of Classical Vortex Generators Now for Transition Delay. *Physical Review Letters* **109** (7), 074501.

Swearingen, J. D. & Blackwelder, R. F. 1986 Spacing Of Streamwise Vortices On Concave Walls. *AIAA Journal* **24** (10), 1706–1709.

Swearingen, J. D. & Blackwelder, R. F. 1987 The Growth And Breakdown Of Streamwise Vortices In The Presence Of A Wall. *Journal of Fluid Mechanics* **182**, 255–290.

Tan-Atichat, J., Nagib, H. M. & Loehrke, R. I. 1982 Interaction Of Free-Stream Turbulence With Screens And Grids: A Balance Between Turbulence Scales. *Journal of Fluid Mechanics* **114**, 501–528.

Taylor, G. I. & Batchelor, G. K. 1949 The Effect Of Wire Gauze On Small Disturbances In A Uniform Stream. *Quaterly Journal of Mechanics and Applied Mathematics* **2** (1), 1–27.

Vaughan, N. J. & Zaki, T. A. 2011 Stability Of Zero-Pressure-Gradient Boundary Layer Distorted By Unsteady Klebanoff Streaks. *Journal of Fluid Mechanics* **681**, 116–153.

Watmuff, J. H. 1998 Detrimental Effects Of Almost Immeasurably Small Freestream Nonuniformities Generated By Wind-Tunnel Screens. *AIAA Journal* **36** (3), 379–386.

Watmuff, J. H. 2006 Effects Of Weak Free Stream Nonuniformity On Boundary Layer Transition. *Journal of Fluids Engineering* **128** (2), 247–257.

Westin, K. J. A., Boiko, A. V., Klingmann, B. G. B., Kozlov, V. V. & Alfredsson, P. H. 1994 Experiments In A Boundary Layer Subjected To Free Stream Turbulence. Part 1. Boundary Layer Structure And Receptivity. *Journal of Fluid Mechanics* **281**, 193–218.

Wundrow, D. W. & Goldstein, M. E. 2001 Effect On A Laminar Boundary Layer Of Small-Amplitude Streamwise Vorticity In The Upstream Flow. *Journal of Fluid Mechanics* **426**, 229–262.